JOURNAL OF GEOPHYSICAL RESEARCH: EARTH SURFACE, VOL. 118, 571–588, doi:10.1002/jgrf.20038, 2013

Modeling past and future surface mass balance of the Northern Patagonia Icefield

M. Schaefer,[1,5] H. Machguth,[2,3] M. Falvey,[4] and G. Casassa[1,6]

Received 20 July 2012; revised 20 November 2012; accepted 29 January 2013; published 6 May 2013.

[1] Glaciers are strongly retreating and thinning in Patagonia. We present new inferences about the climatic situation and the surface mass balance on the Northern Patagonia Icefield in the past and the future using a combined modeling approach. The simulations are driven by NCAR/NCEP Reanalysis and ECHAM5 data, which were physically downscaled using the Weather Research and Forecasting regional climate model and simple sub-grid parameterizations. The surface mass balance model was calibrated with geodetic mass balance data of three large non-calving glaciers and with point mass balance measurements. An increase of accumulation on the Northern Patagonia Icefield was detected from 1990–2011 as compared to 1975–1990. Using geodetic mass balance data, calving losses from the Northern Patagonia Icefield could be inferred, which doubled in 2000–2009 as compared to 1975–2000. The 21st century projection of future mass balance of the Northern Patagonia Icefield shows a strong increase in ablation from 2050 and a reduction of solid precipitation from 2080, both due to higher temperatures. The total mass loss in the 21st century is estimated to be 592 ± 50 Gt with strongly increasing rates towards the end of the century. The prediction of the future mass balance of the Northern Patagonia Icefield includes several additional sources of errors due to uncertainties in the prediction of future climate and due to possible variations in ice dynamics, which might modify the geometry of the icefield and change the rate of mass losses due to calving.

Citation: Schaefer, M., H. Machguth, M. Falvey, and G. Casassa (2013), Modeling past and future surface mass balance of the Northern Patagonia Icefield, *J. Geophys. Res. Earth Surf.*, *118*, 571–588, doi:10.1002/jgrf.20038.

1. Introduction

[2] The Patagonian Icefields constitute the largest ice masses in the Southern Hemisphere outside of Antarctica. The great majority of the glaciers have been retreating and thinning in recent decades [*Naruse et al.*, 1997; *Rignot et al.*, 2003; *Rivera et al.*, 2007; *Masiokas et al.*, 2009; *López et al.*, 2010; *Willis et al.*, 2012]. Very little is known about how these changes in ice mass are connected to changes in climate: Do glaciers loose mass due to increased melt, decreasing accumulation, changes in the ice dynamics or a combination of all of these contributions?

[3] Different signals of climate change have been observed in the region of the icefields: Analyzing seven meteorological stations distributed on both the eastern and the western sides of the icefields *Rosenblüth et al.* [1995] observed a warming trend of 0.4°C–1.4°C (0.003°C–0.028°C/year) south of 46°S since the beginning of the last century, with highest warming at Rio Gallegos next to the Atlantic ocean. *Ibarzabal y Donangelo et al.* [1996] found a warming trend of 0.3°C in the period 1940–1990 (0.006°C/year) at a weather station in El Calafate (50°30'S) close to the Moreno Glacier, a large outlet glacier of the Southern Patagonian Icefield. Analyzing reanalysis data at the grid point 50°S, 75°W, *Rasmussen et al.* [2007] found a warming of 0.5°C at 850 hPa between 1960 and 1999 (0.013°C/year). *Falvey and Garreaud* [2009] found that between 38°S and 48°S temperature trends over land were weak in the last 30 years. As for precipitation, large inter-annual and interdecadal variations have been observed in Patagonia, although with no significant overall trends in the last century [*Rosenblüth et al.*, 1995; *Carrasco et al.*, 2002; *Aravena and Luckman*, 2009].

[4] Geodetic mass balance observations have reported high thinning rates for the ablation region [*Rignot et al.*, 2003]. More recently, significant thinning, although at smaller rates than in the ablation areas, has also been observed over the accumulation region [*Rivera et al.*, 2007; *Willis et al.*, 2012; *López and Casassa*, 2011]. Glaciological

[1]Centro de Estudios Científicos, Valdivia, Chile.
[2]Department of Geography, University of Zurich, Zurich, Switzerland.
[3]Geological Survey of Denmark and Greenland Copenhagen, Copenhagen, Denmark.
[4]Department of Geophysics, Universidad de Chile, Santiago, Chile.
[5]Now at Instituto de Ciencias Físicas y Matemáticas, Facultad de Ciencias, Universidad Austral de Chile, Valdivia, Chile.
[6]Now at Geoestudios, Las Vertientes, San José de Maipo, Chile and Universidad de Magallanes, Dirección de Programas Antárticos y Subantárticos, Punta Arenas, Chile.

Corresponding author: M. Schaefer, Instituto de Ciencias Físicas y Matemáticas, Facultad de Ciencias, Universidad Austral de Chile, Valdivia, Chile. (mschaefer@uach.cl)

2169-9003/13/10.1002/jgrf.20038

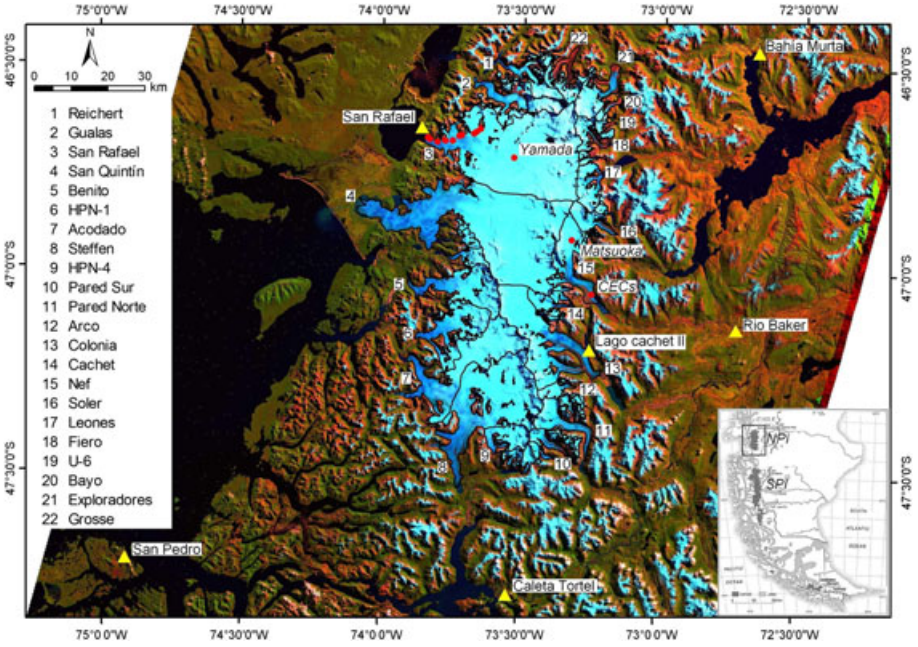

Figure 1. The Northern Patagonia Icefield (NPI). False-color composite of Landsat ETM+ satellite images mosaic, bands 1 (red), 4 (green) and 5 (blue), acquired on 11 March 2001. The numbered major glacier catchments are taken from *Rivera et al.* [2007]. Yellow triangles represent weather stations that were used for the validation of the modeled climate data and red points represent direct mass balance measurements on the NPI. Inset: Location of the NPI and SPI in Southern South America.

mass balance observations include ablation data measured at stakes [*Ohata et al.*, 1985; *Takeuchi et al.*, 1996] and accumulation data from firn cores [*Yamada*, 1987; *Aristarain and Delmas*, 1993; *Matsuoka and Naruse*, 1999; *Schwikowski et al.*, 2006; *Kohshima et al.*, 2007; *Vimeux et al.*, 2008].

[5] Mass balance modeling efforts on the icefields are sparse: *Rivera* [2004] applied a degree model to Chico Glacier on the Southern Patagonia Icefield to calculate the surface ablation and distributed accumulation according to a precipitation lapse rate derived from short-term observations of accumulation at three points in the accumulation area and in the vicinity of the glacier. Using data from reference stations located around the periphery of the Patagonian Icefields as input, he obtained an average annual surface mass balance of -0.84 ± 0.30 m/yr for Chico Glacier for the years 1975–2001. *Koppes et al.* [2011] applied a degree-day model and estimated an accumulation gradient, considering the accumulation measurements of *Yamada* [1987] and *Matsuoka and Naruse* [1999], to model the surface mass balance of San Rafael Glacier. Using reanalysis data as input for the mass balance model, they obtained a slightly positive average annual surface mass balance for the period 1960–2005. Comparing ice elevation changes and length changes of the glacier with the results of the mass balance model, they could make inferences about the calving fluxes of the glacier.

[6] In this contribution, we examine the climate and the surface mass balance on the Northern Patagonia Icefield (Figure 1), using a combined modeling approach based on NCEP/NCAR reanalysis data [*Kalnay et al.*, 1996] and the ECHAM5 Global Circulation Model data [*Roeckner et al.*, 2003] similar to the approach presented in *Machguth et al.* [2009] for the Alps. A physical downscaling of these data sets to a resolution of 5 km is achieved by applying the regional Weather Research and Forecasting (WRF) climate model on a test period (2005–2011). Analyzing the test period, generalized downscaling patterns can be recognized and applied to the rest of the data set (section 2.1). The physically downscaled meteorological data are further downscaled to a resolution of 450 m by sub-grid parameterizations, which consider constant temperature and precipitation gradients and clear-sky radiation calculations [*Corripio*, 2003] on the finer grid. The surface mass balance model considers the incoming solar radiation, along with a term that approximates the sum of the long-wave radiation and the turbulent fluxes using a linear function in temperature [*Oerlemans*, 2001] (section 2.2). The results of the downscaling of climate data are compared to measurements at different weather stations and corrected for observed biases (section 3). In section 4, the results of the surface mass balance simulations from 1975 to 2011 are presented and compared to mass balance observations. In section 5, predictions are made for the surface mass balance of the Northern Patagonia Icefield in the 21st century. In section 6, we discuss our results and draw the major conclusions of our work.

1.1. The Northern Patagonia Icefield

[7] The Northern Patagonia Icefield (NPI) with an area of 3953 km^2 [*Rivera et al.*, 2007] (Figure 1) and the Southern Patagonia Icefield (SPI) with an area of 13,000 km^2 [*Aniya et al.*, 1996] (inset Figure 1) are the two largest ice masses in the Southern Hemisphere outside of Antarctica. They lie at relatively low latitudes (46°30'S–51°30'S) as compared to other glaciated regions with maritime influence (Alaska or Northern Europe) and San Rafael Glacier on the NPI is

the nearest tidewater calving glacier to the equator. On the NPI, San Rafael is the only tidewater calving glacier and several other glaciers calve into rather small pro-glacial lakes. On the SPI, most of the major outlet glaciers calve into fjords on the western side and into large lakes on the eastern side of the icefield. Both icefields together contributed 0.042 ± 0.002 mm per year to sea-level rise during the period 1968/1975–2000 [*Rignot et al.*, 2003], the NPI accounting for 27% of this amount. Ice thicknesses on the plateau of the NPI are very high (up to 1460 ± 500 m, *Casassa* [1987]).

[8] Due to the harsh climatic conditions and large mass turnover rates on the NPI, direct mass balance measurements are difficult to accomplish. A Japanese expedition in December 1983 installed ablation stakes from an altitude of 200–1000 m above sea-level at San Rafael Glacier [*Ohata et al.*, 1985]. On Nef Glacier, Centro de Estudios Científicos (CECs),Valdivia, Chile, started a measurement campaign in 2008 and summer ablation was measured since the 2008/2009 summer. Two mass balance values from the accumulation areas of Glacier San Rafael and Glacier Nef, were obtained by analyzing shallow firn cores [*Yamada*, 1987; *Matsuoka and Naruse*, 1999].

[9] Two important geodetic mass balance surveys including the NPI are used in this contribution in order to validate the output of the model:

[10] 1. *Rignot et al.* [2003] compared a DEM generated from maps compiled by the Instituto Geográfico Militar of Chile generated from aerial photographs of the year 1975 and Argentinean cartography from 1968 with the DEM from the 2000 Shuttle Radar Topography Mission (SRTM DEM).

[11] 2. *Willis et al.* [2012] compared the same 2000 SRTM DEM with different DEMs generated from ASTER images between 2007 and 2011. They generated a time series of elevation changes with the different DEMs generated from the ASTER images. The average time between the ASTER DEMs and the SRTM DEM is denoted as 9.2 years.

2. Methods

2.1. Downscaling of Global Meteorological Data

[12] Obtaining realistic meteorological input data for surface mass balance modeling over the Patagonian Icefields is a major challenge. The Patagonian Andes are high, narrow and complex mountain ranges that mark an extremely sharp climatological gradient. On the western side of the icefields, precipitation records from weather stations at lighthouses and isolated coastal townships indicate annual rainfall of between 2–6 m, with little seasonal variation [*Carrasco et al.*, 2002]. East of the divide, annual precipitation drops rapidly and may be less than 0.3 m only tens of kilometers from the crest. At elevated sites over the icefields themselves, precipitation records are sparse. Very high accumulation values are estimated to balance the high ablation rates observed at the tongues of the outlet glaciers [*Ohata et al.*, 1985; *Takeuchi et al.*, 1996; *Rott et al.*, 1998]. Mean annual precipitation rates in the range of 5–8 m were derived analyzing the discharges measured in the main rivers of the principal catchments of the icefields [*Peña and Escobar*, 1987; *Escobar et al.*, 1992]. *Shiraiwa et al.* [2002] measured accumulation of 17.8 m/yr between the summers 1997/1998 and 1998/1999 in the accumulation area of Tyndall Glacier on the SPI analyzing a shallow firn core.

[13] The extremely high accumulations over the Patagonian Icefields are a direct consequence of orographic precipitation processes [*Smith*, 1979; *Roe*, 2005; *Houze*, 2012] that occur as the prevailing westerlies force moist air to rise up over the mountains. In the most simple upslope flow formulations, the amount of precipitation is proportional to the incoming moisture flux multiplied by the slope of the underlying terrain [*Lin et al.*, 2001]. Consistently, studies in several mountain ranges around the world have shown strong empirical relationships between orographic precipitation and flux related parameters observed upstream [*Wratt et al.*, 2000; *Pandey et al.*, 1999; *Falvey and Garreaud*, 2007]. *Garreaud et al.* [2012] used a medium resolution mesoscale model to explore precipitation forcing over Patagonia and found a strong relationship between simulated rainfall and low-level zonal flow along the western side of the Patagonian Andes. The amount of precipitation may also depend on other factors such as the timescales for hydrometeor formation [e.g., *Jiang and Smith*, 2003], and the vertical extent of the upslope flow. The former is related to the efficiency of the microphysical processes within the orographic cloud (which in turn has a strong link to air temperature), while the latter depends largely on the speed and stability of the impinging flow.

[14] Due to its narrow width (around 50 km), orographic precipitation processes over the NPI are not represented in current GCMs used for climate change simulations. For example, the entire NPI fits beneath just one grid cell of the ECHAM5 used to simulate future climate in the present study. As such, the use of downscaling methods is necessary if realistic input data for mass balance calculations are to be obtained. Downscaling methods are generally divided into statistical or dynamical categories. Statistical downscaling techniques usually relate local observations to the large scale circulation parameters that are well predicted by general circulation models (GCMs) using either weather typing, weather generators or regression models [*Wilby and Wigley*, 1997]. In all of these methods, regional climate is considered to respond to the large-scale climate state in the form $R = \mathrm{F}(X)$, where R represents the local climate variable that is being downscaled, X is the set of large-scale climate variables (predictors) and F is a function that is established by training and validating the models using point observations or gridded reanalysis data. Statistical methods require that long observational data sets be available in order to develop reliable models F, and the technique is of limited applicability in regions where observing networks are sparse.

[15] The total absence of reliable, long-term observational records over the NPI means that the use of dynamical downscaling methods, based on regional climate models (RCMs) is the only alternative for generating physically plausible patterns of surface meteorological forcing. RCMs are limited area models that resolve a complete set of dynamical equations for atmospheric motion, taking into account the impact of topography at a scale determined by the resolution (grid spacing) of the computational domain. Lateral boundary conditions are usually provided by the output from global analysis or GCM simulations of past, present or future climates, depending on the study objective. A drawback of

all RCMs is their high computational cost, which increases dramatically as horizontal resolution is improved, and carrying out long-term simulations with high resolution RCMs is often not feasible.

[16] Our study objective is to provide simulations of the mass balance over the NPI for the period 1975–2100 based on daily surface meteorological data. Unfortunately, neither the computational resources nor enough long-term observational data sets are available that would allow the direct application of either a high resolution RCM or statistical downscaling techniques. We have therefore opted for a somewhat unconventional approach that uses a RCM to provide high resolution (5 km) simulations over the NPI for a limited 7 year time period (2005–2011). Statistical downscaling techniques are then used to develop regression equations that relate RCM predictions to large scale atmospheric parameters available in all global models and reanalysis. These equations are then applied to NCEP/NCAR reanalysis data to extrapolate backwards over the period 1975–2011, and forwards for the period 2000–2100 using simulated weather data from the ECHAM5 GCM.

2.1.1. Dynamical Model (2005–2011)

[17] The Weather Research and Forecasting (WRF) regional atmospheric model constitutes the dynamical component of our downscaling scheme. WRF is a modern, widely used atmospheric simulation code appropriate for spatial scales ranging from several hundreds of meters to several thousands of kilometers. The model employs a non-hydrostatic dynamical core [*Skamarock and Klemp*, 2008] along with a number of physical parameterization schemes for cloud, rain and snow/ice processes, surface interactions, planetary boundary layer (PBL), radiative transfer, and turbulence. The WRF model has been used for downscaling purposes in past studies [*Bukovsky and David*, 2009], and has also been successfully employed to simulate orographic precipitation processes in several mountain ranges worldwide (e.g., *Houze* [2012] and references therein). In this study, version 3.2 of the WRF-ARW (Advanced Research WRF) model was run for a 7 year period from 2005 until 2011, using a nested computational grid with a spatial resolution of 5 km over an area of 675 km × 425 km that includes both the NPI and SPI. Here, we focus on the NPI only, but data from the entire model domain are used to validate precipitation and temperature fields against available observational data in the region (section 3). Figure 2 shows the topography of the model over the NPI.

[18] The model was forced at its boundaries by NCEP-NCAR atmospheric reanalysis [*Kalnay et al.*, 1996]. These analyses combine information from operational meteorological observing systems with a coarse resolution dynamical model to produce spatially and temporally consistent 3-D atmospheric fields on a 2.5° resolution grid at 6 h intervals. To simulate precipitation, the WRF simulations made use of the Thompson bulk micophysics scheme, which simulates interactions between five phases of liquid and solid water in the atmosphere [*Thompson et al.*, 2008]. Other parameterization schemes employed include the surface layer and PBL scheme of *Sukoriansky et al.* [2005], Kain-Fritsch convection [*Kain and Fritsch*, 1993] (outer grids only), and shortwave/longwave radiation by *Chou and Suarez* [1994] and *Mlawer et al.* [1997], respectively. WRF output was

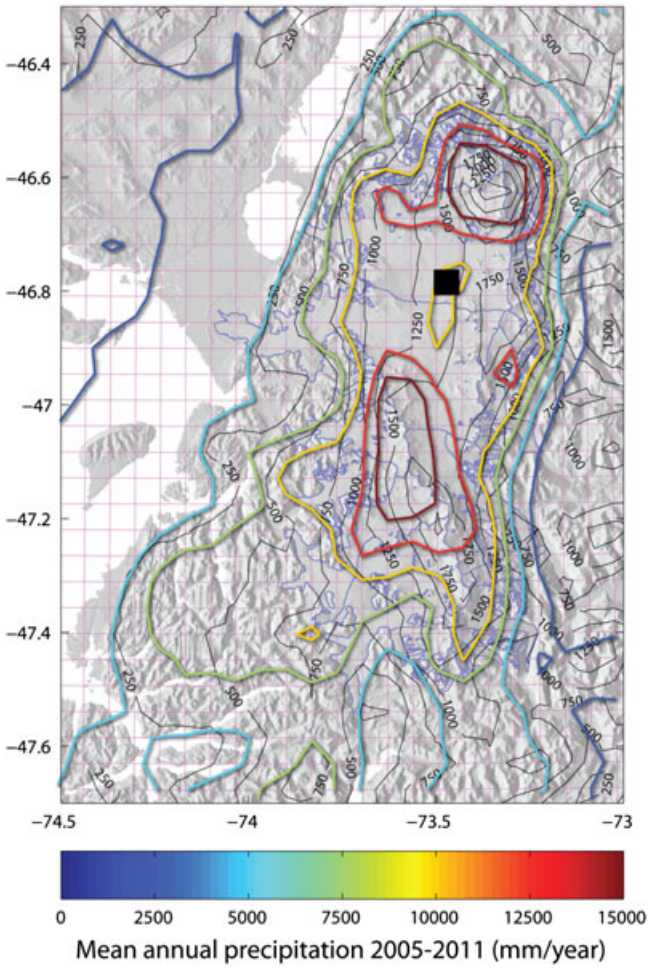

Figure 2. WRF model 5 km grid (pink lines) and model topography (black contours in m a.s.l.) including the Northern Patagonian Icefield (blue lines). The background shaded relief indicates the real topography derived from the 90 m resolution SRTM global database. Colored contours indicate the mean annual precipitation simulated by WRF for the period 2005–2011 (contour lines every 2500 mm). The black square shows the model grid point used in the examples shown in Figure 3.

saved at hourly intervals and later processed to yield the daily averages required by the mass balance model described in section 2.2. The long-term pattern of precipitation produced by the WRF model is shown in Figure 2 and indicates a considerable degree of variability across the NPI. The mean annual accumulations predicted by WRF are very high, reaching over 15 m in highest elevation parts of the NPI. A detailed discussion of the accuracy of these precipitation fields, along with the temperature and incoming solar radiation data that are also derived from the WRF model, is presented later in section 3.

2.1.2. Statistical Extrapolation (1975–2011)

[19] Statistical downscaling techniques are usually used to relate local climate observations to large scale atmospheric parameters that are predicted by low resolution GCMs [*Fowler et al.*, 2007]. In this study, we apply the same techniques to climate variables derived from the WRF

Table 1. Predictor Set Used to Develop Regression Equations[a]

Variable	Description	Pressure Levels (hPa)	Units	Mean: 2000–2011 (Reanalysis)	Mean: 2000–2011 (ECHAM5)	Trend: 2000–2100 (ECHAM5)
T	Atmospheric temperature	1000	K	282	282	+1.8
		700		266	264	+2.9
		300		226	223	+4.0
RH	Relative humidity	1000	%	76	75	–0.8
		700		58	51	–2.0
Fu	Zonal moisture flux	1000	kg/(s m^2)	0.031	0.018	+0.004
		700		0.027	0.032	+0.007
		300		0.003	0.003	+0.001
Fv	Meridional moisture flux	1000	kg/(s m^2)	–0.012	–0.018	—
		700		0.001	0.001	—
		300		0.000	0.000	—

[a]The mean values of each predictor are shown for both NCEP/NCAR Reanalysis and the ECHAM5 for the period 2000–2011. The final column gives the long-term trends in each predictor simulated by ECHAM5 during the period 2000–2100, expressed as the change in the predictor per 100 years. Only significant (P = 0.05) trends are shown.

simulations. The basic assumption is that local variability (which in this case is simulated rather than observed) is to a large extent controlled by the overriding synoptic condition, and that long-term changes in these synoptic conditions are the key drivers of long-term changes in local variables. Given that the reanalysis data to be used to train the statistical model are the same as that used to specify the lateral boundaries of the WRF model, we expect to find strong statistical relationships even though only 7 years of WRF data are available. In this study, we adopt a straightforward multiple-regression technique, in which linear equations were developed separately at each model grid point (i,j) for each of the three variables R required by the mass balance model (daily precipitation, temperature, and solar radiation). The daily R_{ij} series for the period 2005–2011 are modeled in terms of 11 predictors (X) taken from the NCEP-NCAR reanalysis at a grid point some 250 km upstream (west) of the NPI. The predictor set is summarized in Table 1 and consists of a mix of atmospheric variables deemed to be most important in orographic precipitation situations, including lateral moisture flux components, humidity and temperature. Because temperature predictors are available at several levels, information regarding atmospheric stability is also included within the predictor set. The single upstream grid point was used because this point is topography free in the Reanalysis model. Meteorological variables at this location are expected to be more comparable to the same variables taken from other models (such as ECHAM5, see section 2.1.3) that may have different topography directly over the NPI.

[20] The coefficients of the linear equations were determined using stepwise regression technique [*Wilks*, 2006], which retains only those predictors whose inclusion explains a significant (p = 0.05) additional fraction of the variance of R_{ij}. In the case of daily precipitation and incoming solar radiation, whose underlying climatological distributions are highly non-Gaussian, a normal-quantile transform *Themeßl et al.* [2011] was applied before applying the regression procedure. Figure 3 shows an example of the downscaling procedure applied to the precipitation series at a model grid point on the upwind slopes of the NPI.

[21] The complete regression equation (not shown) for precipitation P at this point includes several predictors of which the most important are +Fu700, +T1000 and –T700. Fu700 is the zonal moisture flux at 700 hPa and T1000 and T700 are the temperature at 1000 and 700 hPa, respectively. Varying these predictors explains 85% of the variance in P. The presence of the Fu700 term is not surprising, as the previously mentioned studies of orographic precipitation have indicated the low level moisture flux perpendicular to the mountain range to be a near ubiquitous controlling factor in mid-latitude mountains. Indeed, the Fu700 term contributes to about 50% of the downscaled precipitation variance. The temperature terms have opposite signs, which indicates that precipitation is also modulated, to a lesser extent, by low level atmospheric stability (e.g., T700–T1000), with higher stability leading to lower precipitation amounts. This result is also physically reasonable, as the vertical extent of upward motion on the upwind slopes is known to increase with decreasing stability [*Smith*, 1979], and convective circulations are inhibited in more stable air masses. At daily time scales, the regression model performs reasonably well in reproducing the WRF precipitation series (Figure 3a), although there is considerable scatter (Figure 3b), reflecting the complexity of the processes that lead to precipitation in the WRF model, and the overall correlation coefficient (r) is 0.76. When collected into monthly averages (Figures 3c and 3d), the correlation improves significantly (r = 0.89) indicating that the statistical downscaling method is well capable of capturing precipitation variability at longer timescales. The lower panel (Figure 3e) shows how the technique may be used to extrapolate the WRF backwards over 1975–2011, by simply applying the regression equations to daily reanalysis data for this period. The resulting annual series show considerable year-to-year variability in precipitation over the icefields, along with a weak increasing trend. Results for near-surface temperature variability (not shown) show much higher correlations (r = 0.91 for daily means) and strong dependence on the temperature in the lower atmosphere (T700). Results for daily mean incoming solar radiation show weaker performance statistics (r = 0.71 at daily time scales), and like the precipitation, show a strong dependency on the moisture flux at 700 hPa. Regression results were developed for each model grid point in the entire WRF computational domain, in order to facilitate the validation of the downscaling system against real observational

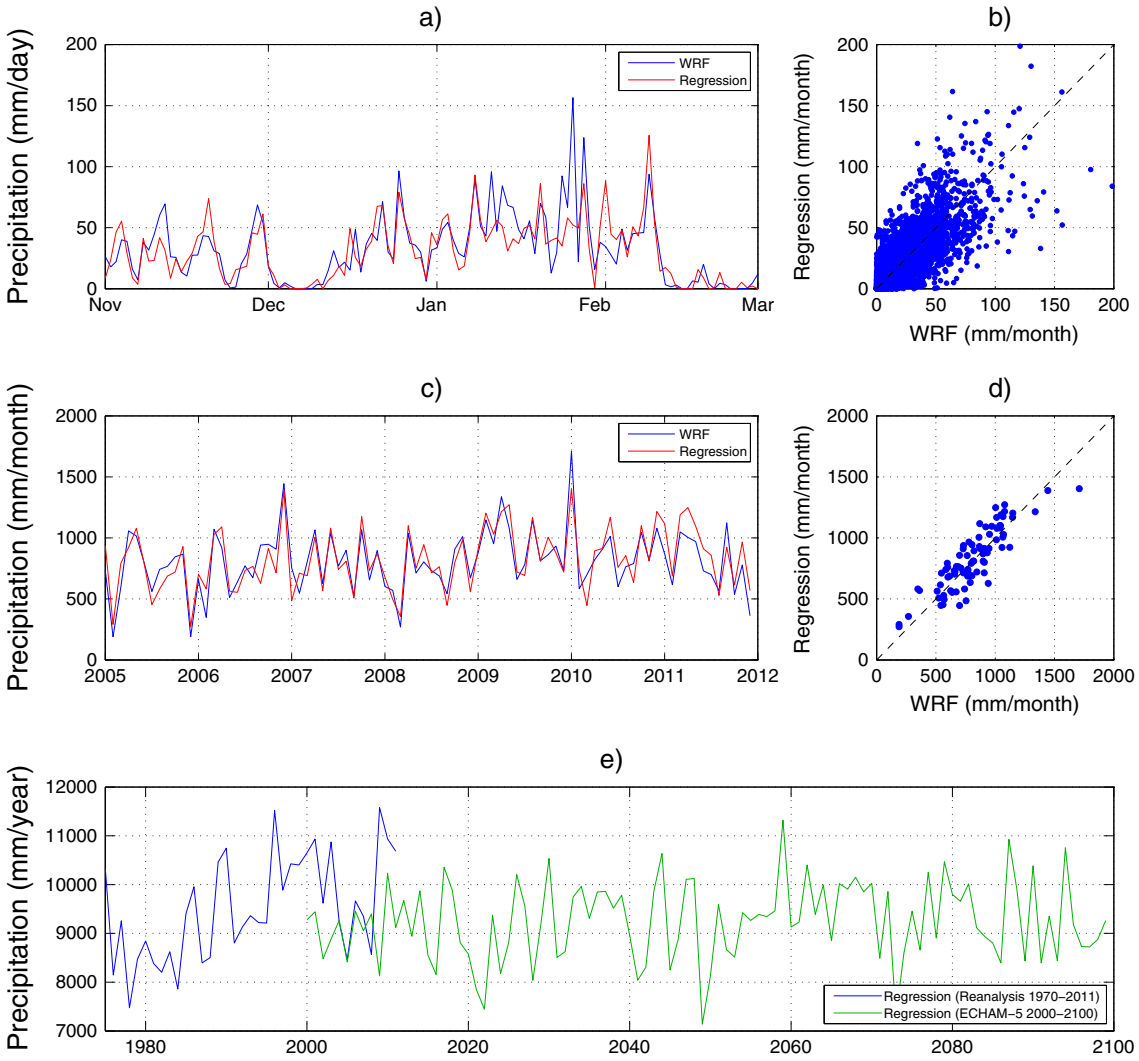

Figure 3. Example of the statistical downscaling procedure for precipitation at the model grid point shown on Figure 2 (46.8°S, 73.5°W). The top panels show (a) the daily precipitation simulated by WRF (blue) and retrieved (red) using the statistical regression procedure for an example 4 month period from November 2009 until March 2010. (b) The scatter diagram for daily precipitation compares daily precipitation for entire period 2005–2011. The middle panels show (c) time series and (d) the scatter diagram of monthly accumulated precipitation from 2005–2011. Finally, (e) shows downscaled annual precipitation series for present climate (1970–2011) and the projection for the 21st century based on the ECHAM5 GCM simulation.

data (section 3). Over all NPI grid points, the correlation coefficients obtained are similar to the previous example (0.65–0.80 for precipitation, 0.85–0.93 for temperature and 0.56–0.77 for solar radiation) and indicate that the statistical technique is applicable over the entire NPI region where the mass balance model is to be applied.

2.1.3. Future Climate Prediction (2000–2099)

[22] The evolution of surface climate over the NPI during the 21st century is modeled by applying the downscaling technique described in the previous section using data taken from a single simulation of the ECHAM5 coupled ocean-atmosphere general circulation model [*Roeckner et al.*, 2003] under the A1B emissions scenario. The A1B scenario assumes globalization with a balanced emphasis on all energy sources. Under this scenario, the mean global CO_2 concentration by the end of the 21st is approximately twice its pre-industrial value [*Houghton et al.*, 2001]. The available model data are global fields of pressure, temperature, specific humidity and zonal and meridional winds on a global, sigma-level grid of approximately 3.75° resolution, at 6 h intervals for the period 2000–2100. It was possible to process the ECHAM5 data to obtain exactly the same predictor set used to train the statistical downscaling procedure. In order to work correctly, it is important that the predictors derived from ECHAM5 exhibit more or less the same mean values as the Reanalysis in current climate, or else the resulting estimates of the downscaled variables will be biased. A cursory examination of large scale fields over the Patagonia region (not shown) indicates that the ECHAM5 model reproduces the mean climate of the region for the

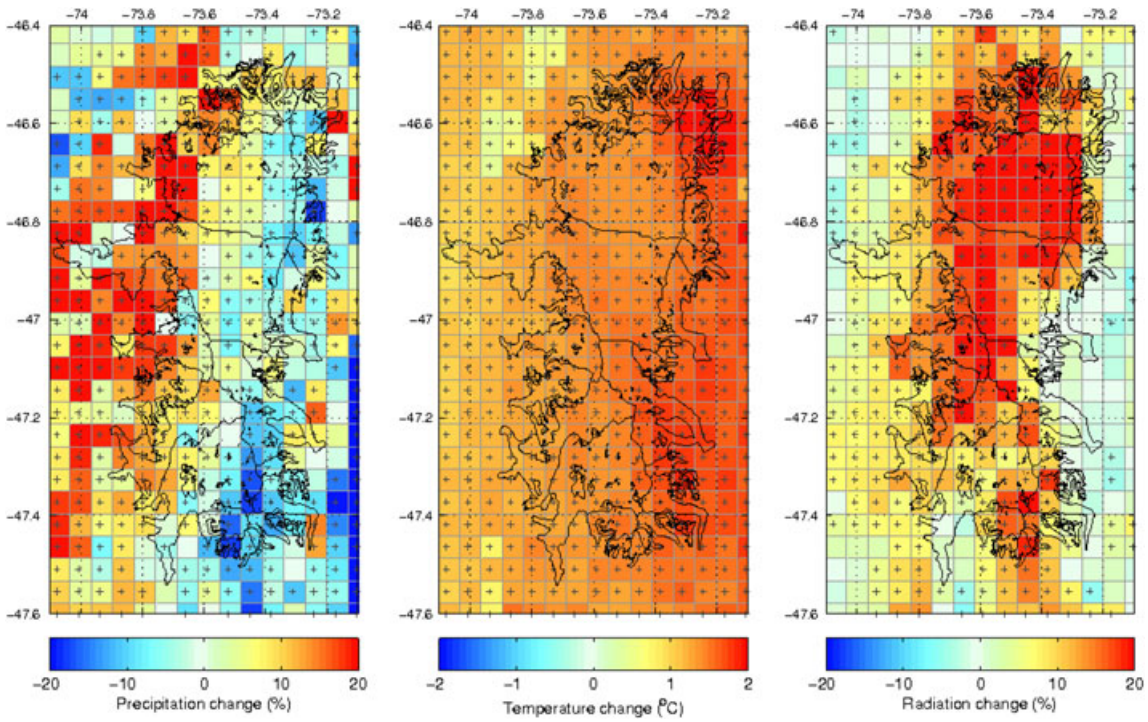

Figure 4. Future climate trends for the period 2000–2100 derived from the application of the downscaling procedure to the ECHAM5 data. (left panel) Precipitation and (right panel) incoming solar radiation trends are expressed as the 100 year percentage change with respect to the mean value. (middle panel) Temperature changes are expressed as degrees per 100 years. Trends were calculated from a straight line fit to the annual time series at each model grid points. Grid points, where the trends are statistically significant (p = 0.05), are marked with a cross.

cross-over period 2000–2011 reasonably well, when both ECHAM5 and Reanalysis data are available. The mean values of the ECHAM5 predictors (Table 1) generally have only small biases and these were subtracted before applying the regression equations.

[23] The downscaling procedure described in the previous section was applied using bias corrected ECHAM5 predictors to generate daily surface data for the period 2000–2100. The precipitation series for the example model grid point used earlier is shown in Figure 3e, where no clear long-term change in annual precipitation may be discerned for this grid point. Figure 4 shows maps of the long-term tendencies in all the meteorological input variables used in the mass balance calculation. Precipitation trends (Figure 4a) are weak over most parts of the NPI, although there is a general spatial pattern of increasing precipitation on the western slopes of the Icefields, and decreasing trends on the main ridges and on the lee side. Overall, the net change in total precipitation over the NPI is small. This behavior is somewhat surprising, as the increasing westerlies predicted by the ECHAM5 model (Table 1) might be expected to lead to higher precipitations over the course of the century. However, it appears that the precipitation increase resulting from stronger moisture fluxes is, to a large extent, canceled out by the effect of increasing low level atmospheric stability upwind of the NPI. Significant increasing temperature trends between 1.5°C and 2.0°C are predicted over all of the NPI for the 21st century (Figure 4b). Incoming solar radiation also shows a significant positive trend (Figure 4c) of between 10–20% over most parts of the NPI.

[24] We note that an important assumption made when using this technique is that the statistical transfer function derived from Reanalysis in present climate remains constant for the future climate simulated by the ECHAM5 model. This is a widely recognized aspect of statistical downscaling methods in general, and its implications have been discussed in several review papers (e.g., *Giorgi and Mearns* [1991]; *Wilby and Wigley* [1997]). In general, it is recommended that statistical downscaling techniques only be applied in situations where the circulation regime does not change markedly between the training period and future climate, and where feedbacks between the atmosphere and the land-surface are unlikely to have an important impact on the local climate variables to be predicted. We believe that in the case of the Patagonian Icefields, the statistical relationships derived from Reanalysis are likely to be quite robust for the 21st century. As evidenced by the trends given in Table 1, the atmospheric circulation pattern, characterized by moist prevailing westerlies in the lower troposphere, does not change dramatically throughout the 21st century. Furthermore, the major land-surface feature of the region is the Icefield itself, and this feature is not expected to have a particularly large impact on the values of variables such as precipitation and radiation, nor is its surface area expected to change to such a degree that local climate could be significantly influenced. Nonetheless, the assumption of temporal stability is an important aspect of the downscaling procedure and in future work could be tested by running regional simulations with the WRF model for the future climate scenario.

2.2. Surface Mass Balance Model

[25] A distributed mass balance model with daily time steps is applied to model the surface mass balance of the icefields. A spatial resolution of 450 m was found to be a good compromise between reproducing significant glacier structures and reasonable computation times. As topography for the mass balance model the digital elevation model (DEM) from the 2000 Shuttle Radar Topography Mission with a resolution of 90 m was averaged over five grid cells. The specific surface mass balance b of every grid cell I of the mass balance model was computed by subtracting the ablation a from the accumulation c:

$$b(I) = c(I) - a(I). \tag{1}$$

Ablation was calculated according to a simplified energy balance model in which the sum of the long-wave radiation and the turbulent fluxes is approximated by a linear function in temperature [*Oerlemans*, 2001] :

$$a(I) = \alpha(I) \times Rad_{\text{in}}(I) + C_1 \times T(I) + C_0, \tag{2}$$

where α is the albedo at the grid cell, T denotes the daily average temperature at two meters, Rad_{in} the daily average incoming solar radiation, and C_1 and C_0 are tuning parameters, which will vary depending on how the sum of the long-wave radiation and the turbulent fluxes on average depend on the temperature. Three different albedo values $\alpha_s = 0.7$, $\alpha_f = 0.45$ and $\alpha_i = 0.3$ are used, depending if the surface of the grid cell consists of snow, firn or ice, respectively. In the model, snow turns into firn after 1 year and into ice after another year. The terms in (2) are in W/m^2 and have to be multiplied by the number of seconds of 1 day and divided by the density of water and divided by the latent heat of fusion of water to obtain the daily mass loss in meter water equivalent (m w eq).

[26] The accumulation of mass at every grid cell $c(I)$ is defined as the solid part of the precipitation (P)

$$c(I) = q(I) \cdot P(I), \tag{3}$$

where $q(I)$ is determined by the temperature in the grid cell as follows:

$$q(I) = \begin{cases} 0 \\ \boxed{\text{if T(I)} > 1.5°\text{C}} \\ \frac{1.5°C - T(I)}{1°C} \\ \boxed{\text{if } 0.5°\text{C} < \text{T(I)} < 1.5°\text{C}} \\ 1 \\ \boxed{\text{if T(I)} < 0.5°\text{C}} \end{cases} \tag{4}$$

[27] To obtain the input data on the 450 m-grid of the mass balance simulations, the downscaled meteorological data obtained from the statistical downscaling have to be further downscaled. The temperature is strongly dependent on the elevation. Therefore, this altitudinal dependence is first removed from the daily temperature data on the 5 km-grid obtained from statistical downscaling ($T^{5\text{km}}$) according to

$$T_0^{5\text{km}} = T^{5\text{km}} - z^{5\text{km}} \times lr_T, \tag{5}$$

with a constant temperature lapse rate of $lr_T = 0.0065$°C/m and the elevation according to the WRF model topography $z^{5\text{km}}$ (Figure 3). Then $T_0^{5\text{km}}$ is interpolated to the 450 m-grid $\left(T_0^{450\text{m}}\right)$ and in the next step the temperature dependence is reintroduced according to the mass balance model's topography on the 450 m-grid ($z^{450\text{m}}$):

$$T^{450\text{m}} = T_0^{450\text{m}} - z^{450\text{m}} \times lr_T. \tag{6}$$

We used inverse distance weighted interpolation to obtain $T_0^{450\text{m}}$ from $T_0^{5\text{km}}$. We emphasize that the constant temperature lapse rate lr_T is only used to distribute the temperature more realistically inside the 5 km grid cells. The overall lapse rate of temperature is determined by the WRF simulations (and the statical downscaling procedure). The daily average of the incoming solar radiation on the 450 m-grid is obtained in the following steps:

[28] 1. the clear-sky direct and diffuse incoming solar radiation is calculated on the 450 m-grid using a radiation code [*Corripio*, 2003];

[29] 2. these values are averaged on the 5 km-grid;

[30] 3. the downscaled global radiation data are divided by the averaged clear-sky radiation to obtain a cloudiness factor;

[31] 4. the computed incoming clear-sky radiation on the 450 m-grid is multiplied by the corresponding cloudiness factor, to obtain the actual daily incoming radiation value.

[32] To obtain precipitation data on the 450 m-grid the statistically downscaled precipitation data are first interpolated to the 450 m-grid (inverse distance weighting as well), then a precipitation lapse rate lr_P is applied to account for the differences between the interpolated WRF model topography and the mass balance model's topography:

$$P^{450\text{m}} = P_{\text{int}}^{450\text{m}} \times \left(1 + \left(z^{450\text{m}} - z_{\text{int}}^{450\text{m}}\right) \times lr_P\right), \tag{7}$$

where the precipitation lapse rate lr_P was set to 5% per 100 m. Again, the constant lapse rate is only used to distribute the precipitation more realistically inside the 5 km grid cells, and the overall precipitation lapse rate is determined by the results of the statistically downscaled WRF simulations.

3. Results and Validation of the Downscaling

[33] For the validation of the modeled climate data, several sources of measured meteorological data were available (here, the term 'modeled climate data' is used to refer to the climate data that were used as input data for the mass balance modeling after the statistical downscaling detailed in section 2.1 and the subgrid parametrization explained in section 2.2):

[34] 1. the Chilean Weather Service (DMC): Continuous data of temperature and precipitation with long-time records although there are problems at some stations in the 2000s,

[35] 2. the Chilean Water Directory (DGA): Precipitation data of mixed quality and record length,

[36] 3. other sources: Including the Chilean Navy, the Argentine Weather Service and the measurements of *Koppes et al.* [2011].

[37] Details for all the weather stations analyzed in our study are summarized in Table 2.

3.1. Temperature

[38] Comparing the available temperature measurements with the modeled data, we observed that at all the weather

Table 2. List of Meteorological Stations That Were Used to Verify the Input Data of the Surface Mass Balance Model

N°	Name	Source	Lat	Lon	Elevation (m)	Data Period	ΔT_{mean}	r_{prec}
1	Puerto Aysén	DMC	45°24’	72°40’	11	T,P: 1975–1995	+1.12°C	0.81
2	Puerto Chacabuco	DGA	45°26’	72°49’	20	P: 1985–1987, 1989–1991, 1994–2011	—	0.71
3	Coyhaique	DMC	45°35’	72°07’	310	T,P: 1975–2010	–0.13°C	0.73
4	Balmaceda	DMC	45°54’	71°43’	520	T,P: 1975–2010	+0.30°C	0.68
5	Bahía Murta	DGA	46°27’	72°40’	240	P: 1994–2011	—	0.76
6	Chile Chico	DMC	46°32’	71°41’	327	T: 1976–2005,P: 1975–2004	–0.35°C	0.46
7	San Rafael	M.Koppes	46°38’	73°51’	8	T,P: Mar 2005–Apr 2006	—	0.72
8	Cabo Raper	Navy	46°49’	75°37’	46	T: 2000–2010, P: Mar 2009–Dec 2010	+0.68°C	0.43
9	Rio Baker	DGA	47°08’	72°43’	160	P: 2004–2011 with gaps	—	0.69
10	Lago Cachet II	DGA	47°11’	73°14’	427	P: Aug 2009–Nov 2009, Apr+May 2010	—	0.76
11	San Pedro	Navy	47°43’	74°55’	25	T: 2000–2010	—	—
12	Caleta Tortel	DGA	47°47’	73°32’	10	P: May 2003–2010	—	0.44
13	Rio Pascua	DGA	48°09’	73°05’	20	P: Jan 2003–2011	—	0.76
14	Puerto Eden	DGA	49°07’	74°24’	10	P: 1998–2010 with gaps	—	0.58
15	El Calafate	AWS	50°18’	72°14’	230	T,P: 2002–2011	+1.41°C	0.21
16	Lago Dickson	DGA	50°49’	73°06’	200	P: 2004–2010 with many gaps	—	0.37

stations, the amplitude of the yearly cycle of the temperature was underestimated. Summer temperatures were too low and winter temperatures too high. The underestimation of the yearly temperature amplitude was stronger at the more continental stations and weaker at stations next to the sea. In order to obtain better agreement with the observed data, we added a sinusoidal temperature correction with an amplitude of 2°C to the modeled temperature data. Corrected and originally modeled monthly mean temperatures together with measured monthly mean temperatures from 1975 to 2004 are shown for Puerto Aysén in Figure 5. In Puerto Aysén, the correction of the modeled data improves the prediction of the summer temperatures in most of the cases. However, in most recent summers, the original modeled temperatures agree sometimes better with the observed temperatures. At the more continental stations (Coyhaique, Balmaceda, Chile Chico) the corrected summer temperatures are still too low. Corrected winter temperatures are still overestimated at these weather stations. However, the influence of too warm winter temperatures on the modeled mass balance is not very high, because in the winter time, ablation events are rare. At the lighthouse weather station Cabo Raper, the corrected summer temperatures are a little bit too high and winter temperatures agree well. So the ideal would be to vary the temperature correction with distance from the sea, but with the few measurements available, it is difficult to quantify this variation. Hence, we prefer to chose a spatially constant temperature correction, which was chosen considering stations at the east and the west of the icefields and Puerto Aysén 120 km to the North of the NPI but with a similar longitude. The correlations between the measured and corrected modeled temperatures were generally high, around 0.8 on the daily data and higher than 0.95 on the corrected monthly data. Corrected modeled yearly mean temperatures were mostly slightly higher than the measured ones, due to the warmer winter temperatures at the continental stations (see Table 2). At the stations San Pedro and San Rafael, it was not possible to evaluate the model’s output, because the corresponding WRF-gridcell was classified as ocean, which strongly reduces the yearly amplitude of temperature variation.

3.2. Precipitation

[39] Comparing the modeled monthly precipitation sums to measurements, we obtained generally good correlation (r_{prec}) of around 0.7 for the data sets with longer records

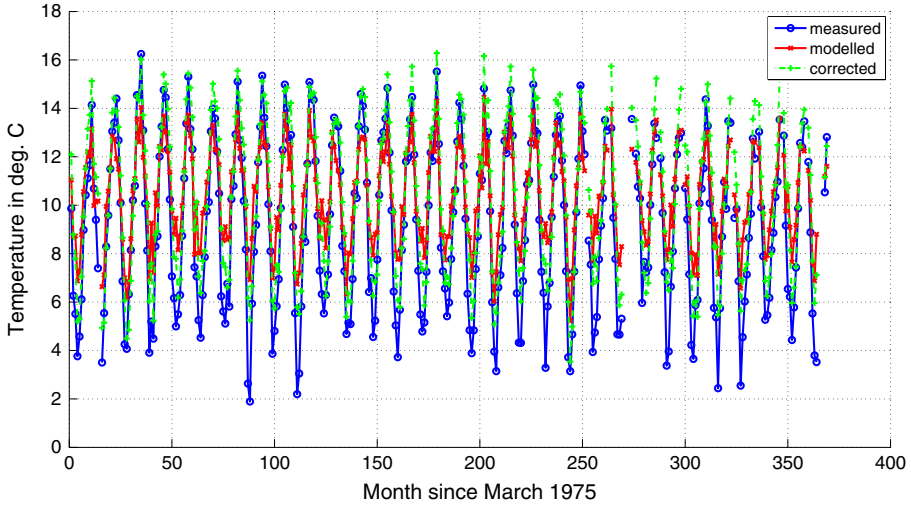

Figure 5. Measured, modeled and corrected monthly mean temperatures in Puerto Aysén from 1975 to 2004.

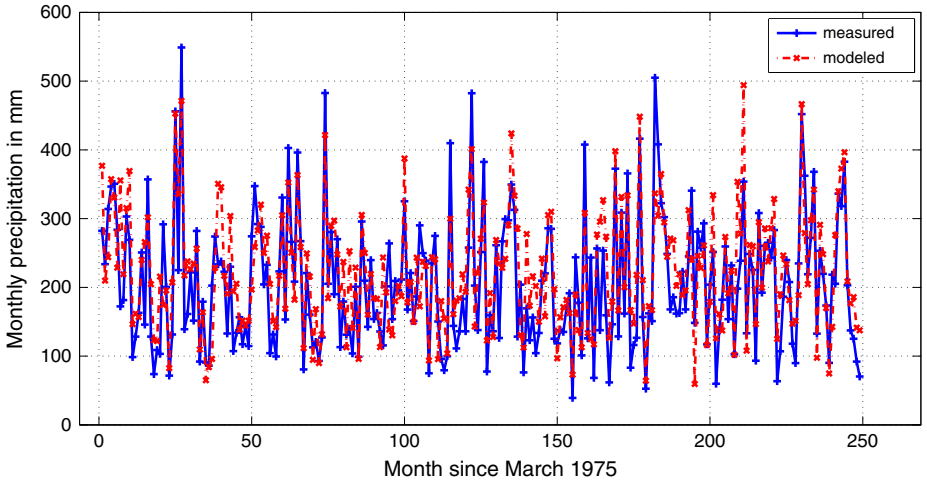

Figure 6. Measured and modeled monthly precipitation at Puerto Aysén weather station.

(Puerto Aysén, Puerto Chacabuco, Coyhaique, Balmaceda, Bahía Murta) (Table 2). In Figure 6, we show the good agreement between the measured and modeled long-term precipitation series of Puerto Aysén.

[40] At the easternmost stations (Chile Chico, El Calafate), where very low amounts of precipitation are registered, the model strongly overestimates the amount of precipitation and the correlations are poor. All in all, it is difficult to find a correction that clearly improves the results of the modeled precipitation data. In most of the cases, we observed an over estimation of the precipitation values and we therefore introduced a global precipitation correction factor $p_{corr} < 1$, which was used as a tuning parameter in the mass balance calculations.

3.3. Incoming Solar Radiation

[41] Unfortunately, only one set of radiation data in the vicinity of the NPI could be obtained. In Figure 7, we present a comparison between modeled and measured incoming solar radiation at the DMC station in Coyhaique between 2005 and 2011. During summer, the modeled radiation shows higher values than the measured radiation of up to 40 W/m^2. Mean values over the presented period, however, where very close (135 W/m^2 modeled and 133 W/m^2 measured). The correlation of the daily values was fairly good as well (r = 0.73). The slightly lower measured radiation values could be due to anthropogenic effects such as air contamination in the vicinity of Coyhaique.

[42] Comparing the results of the clear-sky radiation code of *Corripio* [2003] with the results of the WRF-simulation on clear summer days, we found the WRF tended to produce higher values for the clear-day incoming radiation at lower elevation or non-glaciated cells, whilst on the NPI itself good agreement was found. The over estimations by the WRF model at lower elevations might be due to overly high land-albedo values on snow-free surfaces. The good

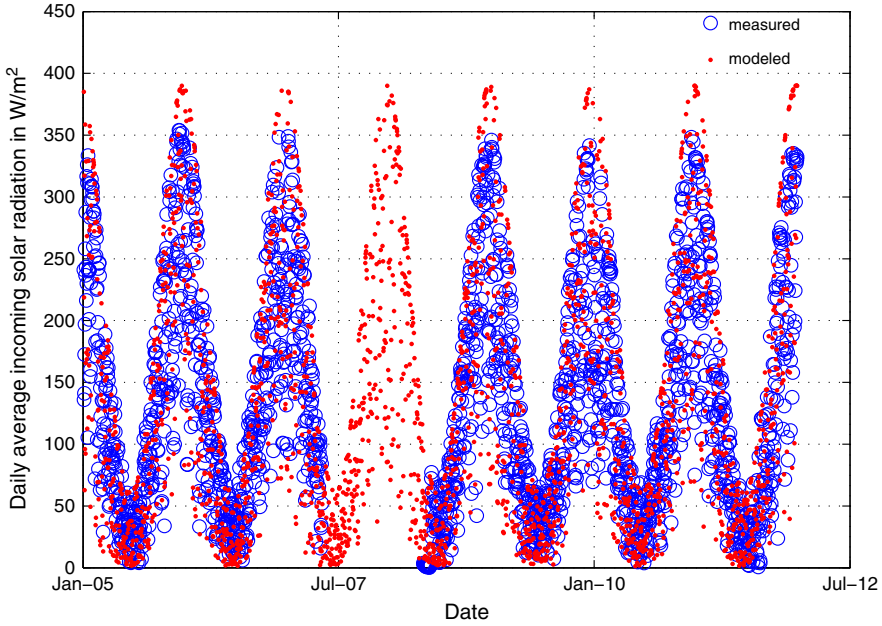

Figure 7. Measured and modeled incoming solar radiation in Coyhaique from 2005 to 2011.

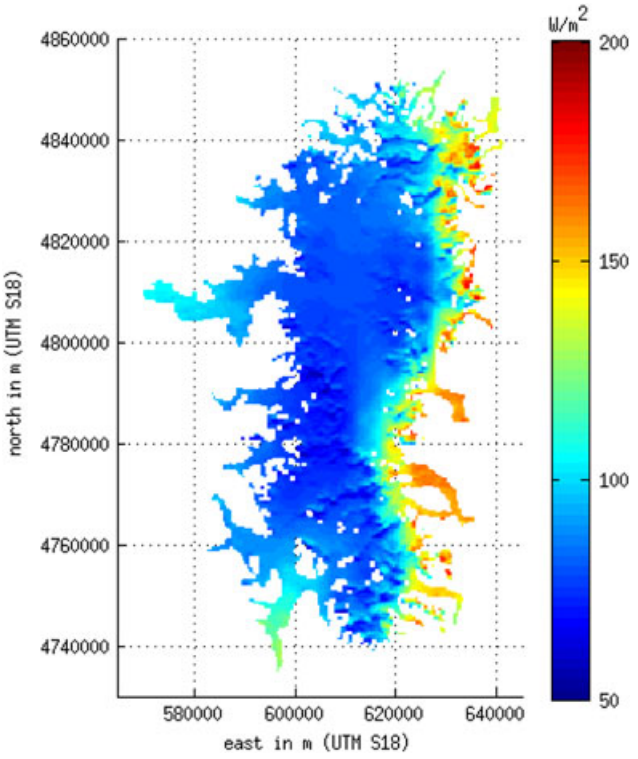

Figure 8. Modeled yearly average incoming solar radiation over Northern Patagonia Icefield between 1975 and 2011.

agreement of the models on the NPI itself makes us confident about the correctness of the radiation values used as input for the surface mass balance model. In Figure 8, we present the long-term pattern of daily incoming solar radiation over the NPI between 1975 and 2011.

[43] The influence of orographic clouds on the western slopes and high peaks of the NPI is easily recognized, which reduce considerably the incoming solar radiation on the western and middle part of the icefield. The amount of radiation is considerably higher on the tongues of the eastern outlet glaciers. On the very western end of the tongue of San Quintín Glacier and on the tongue of Steffen Glacier in the south, an increase of incoming solar radiation is also visible.

4. Results of the Surface Mass Balance Model

4.1. Calibration of the Model and Determination of Uncertainties

[44] As outlined in section 2, the models used to predict the mass balance of the NPI involve the mathematical description of physical processes which take place in nature. This description, however, can only be a simplification of the processes that take place in the atmosphere and on the surface of the glaciers. Therefore, a calibration of the model is necessary. There are three open parameters that allow for a calibration of the model: p_{corr} the precipitation correction factor and C_1 and C_0, which quantify linear dependence of the sum of the long-wave radiative balance and the turbulent fluxes on the temperature. These parameters are, a priori, independent and can be varied systematically to improve the performance of the model. In Table 3, we detail nine sets of parameters, which have been used for the simulation of the surface mass balance of the NPI.

[45] To judge the performance of the parameter sets, the results of the simulation were compared to measurements. Two important geodetic mass balance surveys and several point mass balance measurements were available to judge the performance of the model parameter sets (see section 1.1). The geodetic mass balance data can be used to judge the results of the models in two ways: assuming that mass changes of the glaciers are dominated by surface processes and calving, we can directly compare the modeled mass balance to the measured one for the non-calving glaciers. For the calving glaciers, calving fluxes c can be inferred from the surface mass balance simulations together with the total mass balance observations according to $Q_c = \Delta V_{surf} - \Delta V_{total}$, where V_{surf} denotes the simulated surface mass balance and V_{total} the measured total geodetic mass balance. Since no long-term observations of calving fluxes exist for the time spans examined by the two geodetic mass balance surveys (1975–2000 and 2000–2009), we did not use the inferred calving fluxes to judge the performance of the model. Sometimes, however, the inferred calving fluxes were negative, which we used as an indicator for a negative performance of the model. The different criteria to judge the performance of the model can not be compared quantitatively. Therefore, we ranked the sets of model parameters in Table 3 according to the four following criteria:

[46] 1. best agreement of the simulated volume change of the three largest non-calving glaciers (HPN-1, HPN-4 and Exploradores) between 1975 and 2000 to the geodetic mass balance of *Rignot et al.* [2003]

[47] 2. best agreement of the simulated volume change of the three largest non-calving glaciers (HPN-1, HPN-4 and Exploradores) between 2000 and 2009 to the geodetic mass balance of *Willis et al.* [2012]

[48] 3. best agreement between the modeled and measured mass balance for all point measurements

[49] 4. lowest absolute value of the sum of negative calving fluxes inferred from the simulations and both the geodetic mass balance surveys for the most important calving glaciers of the NPI (San Rafael, San Quintín, Steffen, Colonia, Nef).

[50] To get the overall performance of the set of model parameters, we summed up the positions for the four different criteria (column 4 in Table 3). We can see that following our evaluation procedure, parameter set *H* performed best, followed by set *B* and set *G*. That is, with the observational

Table 3. Definition of the Sets of Model Parameter

	p_{corr}	C_0 in W/m^2	C_1 in W/(m^2*K*)	Sum of Rankings
A	0.78	–45	11.5	19
B	0.78	–40	11	17
C	0.78	–35	10.5	22
D	0.75	–45	11.5	20
E	0.75	–40	11	22
F	0.75	–35	10.5	28
G	0.72	–50	11.5	18
H	0.72	–45	11	16
I	0.72	–40	10.5	17

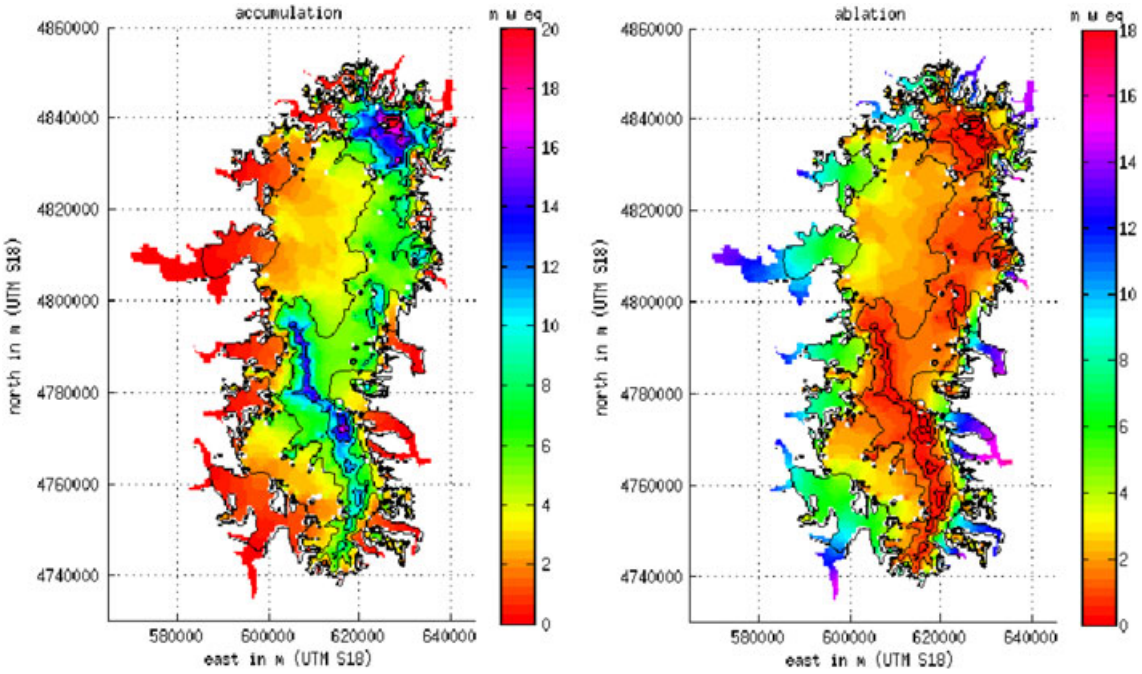

Figure 9. Spatial distribution of yearly accumulation (left) and ablation (right) over the NPI, average 1975-2011 (parameter set *H*) in m w eq; contour lines represent the DEM of the mass balance model and are spaced every 500 m.

mass balance data that were available to us, we can state that these three sets of model parameters reproduced best the observed mass changes on the NPI. By comparing the results of this three model parameter sets, we can get an idea about the sensitivity of the results to the open model parameters, i.e., the reliability of the results.

4.2. Specific Mass Balance

[51] The long-term pattern of yearly specific accumulation and ablation over the NPI averaged over the last 26 years, obtained from the surface mass balance model using parameter set *H* is presented in Figure 9. Very large accumulation values of over 15 m w eq per year were obtained for the high peaks of the NPI with individual point values reaching nearly 24 m w eq on the peak of Mount San Valentín. At an elevation of 1500–2000 m, the accumulation is between 5 m w eq and 10 m w eq. On the large plateaus of the glaciers San Rafael and San Quintín (at an elevation of 1000–1500 m), the accumulation is between 2 and 5 m w eq. On the tongues of the glaciers, the accumulation is very small, because nearly all of the precipitation falls as rain. On average between 1975 and 2011, 51% of the total precipitation over the NPI is rainfall.

[52] Ablation is highest on the tongues of the Eastern outlet glaciers reaching nearly 18 m w eq on the tongue of Colonia Glacier. On the tongue of the southern outlet glacier Steffen, it reaches 15 m w eq, and on the Western outlet glaciers, 14 m w eq. The ablation on the plateau of the glaciers San Rafael and San Quintín is between 2 and 4 m w eq and even on the highest peaks of the NPI, some ablation is possible.

[53] The average annual specific mass balance of the years 1975 to 2011 (again for model parameter set *H*), are presented in Figure 10.

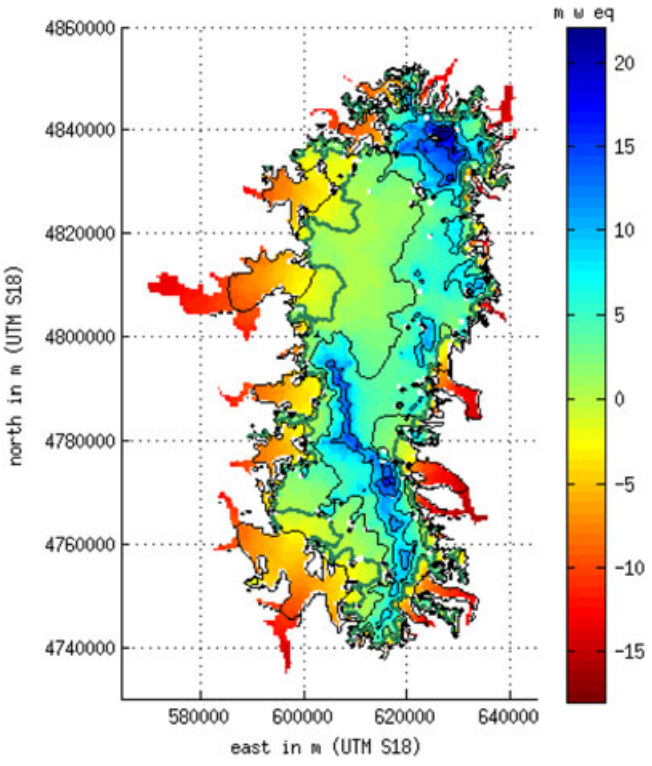

Figure 10. Long-term pattern of the annual specific mass balance of the NPI between 1975 and 2011. The green line denotes the Equilibrium Line, where the specific mass balance is zero. Contour lines represent the DEM of the mass balance model and are spaced every 500 m.

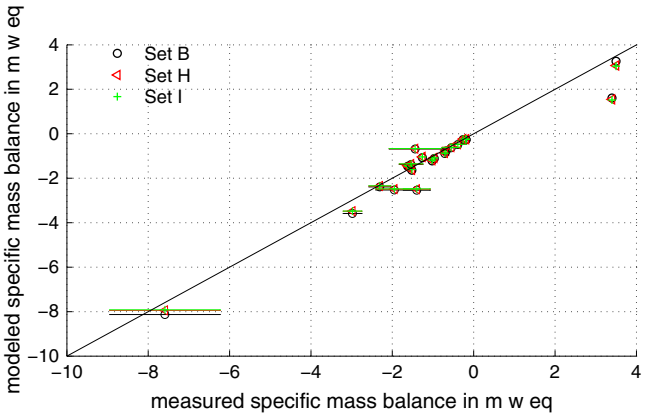

Figure 11. Comparison of modeled mass balance values (model parameters sets *B*, *H* and *I*) with measurements. Ablation measurements at Nef Glacier represent an average of 4–6 stakes (depending on the season) and the error bar represents the standard deviation. The straight line represent equality.

[54] Maximum mass balance values agree with maxima in accumulation, and minima in the mass balance with maxima in ablation. On the plateau, the mass balance is between –2 and 3 m w eq. On the western side, the Equilibrium Line (EL) of zero mass balance is located on the flat parts of the glaciers between 1000 and 1500 m. On the eastern side, the EL is slightly higher and the topography at the EL is steeper on average. The ablation, accumulations and surface mass balance patterns of the model parameters sets *B* and *I* are qualitatively and quantitatively very similar to the results of set *H*.

[55] The results of the simulations of the specific mass balance is compared to the different available point mass balance measurements (see section 1.1) in Figure 11.

[56] For the CECs measurements at Nef Glacier, one point represents the average of 4–6 stakes (depending on the season) and the variability of the results is represented by the error bars. The coordinates of the positions of the Japanese 1983 expedition were estimated with the help of a map in *Nakajima* [1985]. Most of the simulated values agree well with the measurements. Parameter set *B* reproduces the mass balance values in the accumulation area better, whilst sets *H* and *I* reproduce better the ablation. The value obtained from *Yamada* [1987] in the accumulation area, however, is not reproduced very well by any of the parameter sets. Here, one has to keep in mind that local effects like drifting snow may increase the measured accumulation drastically at some places and reduce it at others. Such local effects are not included in the model and probably cancel out over larger areas such as entire glacier catchments, which will be analyzed in the next section.

4.3. Annual Surface Mass Balance of the Individual Glaciers

[57] *Rivera et al.* [2007] recently defined new ice divides for the NPI on the basis of a Digital Elevation Model generated from a mosaic of three ASTER images acquired on 3 September 2001 and ice flow surface patterns that were analyzed on different satellite images. We used catchments defined on the basis of these ice divides to analyze the annual mass balance of the individual glaciers of the NPI. In Figure 12, we present the 1975–2011 average annual surface mass balance of the most important catchments of the NPI obtained for the parameter set *H*.

[58] The only tidewater calving glacier, the San Rafael Glacier has a clearly positive average annual mass balance of 1.6 m w eq. San Quintín, the largest glacier of the NPI, has a slightly negative annual mass balance of –0.5 m w eq. The freshwater calving glaciers Steffen in the south and Nef in the east, show clearly negative mass balances of –1.2m̃ w eq and –1.4 m w eq respectively, which agrees with their strong retreats observed in the last decades [*López et al.*, 2010]. HPN-1 Glacier, the largest non-calving glacier of the icefield has a very negative annual mass balance of –1.9 m w eq, whilst Colonia Glacier, the largest freshwater calving glacier on the eastern side of the NPI has an annual surface mass of approximately zero. The glaciers Pared Norte y Pared Sur in the southeast show extremely low annual mass balance of less than –3 m w eq, which seem to be unrealistically low. Possible reasons could be that these glaciers obtain snow by wind drift from their neighboring glaciers, which show more positive annual mass balances (Arco, HPN-4). Another reason could be that in that part of the icefield, the WRF simulation underestimates the precipitation, as we noted in the nearby weather station in Caleta Tortel (see Figure 1). The very small glaciers Bayo and U6 in the northeast of the NPI show very low annual mass balance values as well. These results have to be interpreted with care since small mistakes in defining the ice divides can cause large errors for small

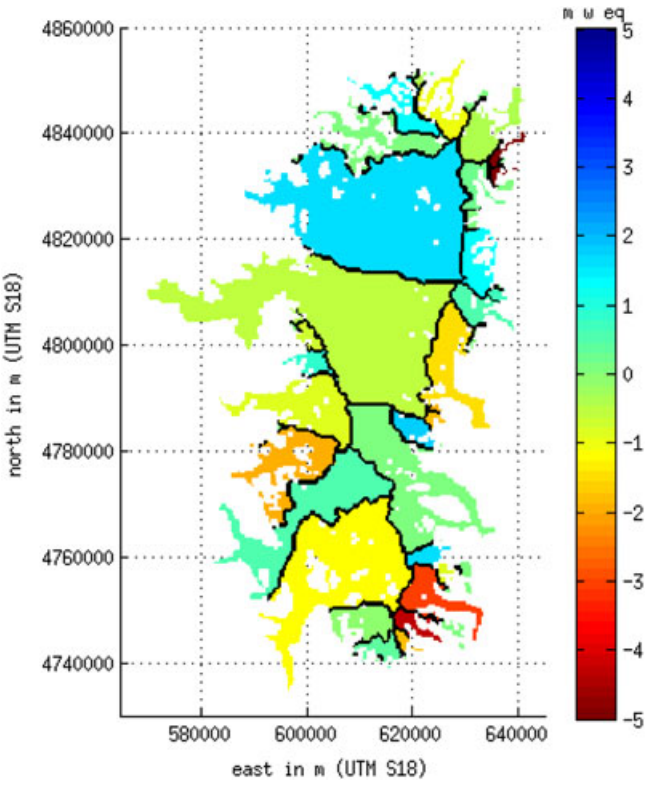

Figure 12. Average annual surface mass balance of the main catchments of the NPI between 1975 and 2011.

Table 4. Measured and Modeled Annual Net Balances (in Meter Water Equivalent) of Three Important Non-Calving Glaciers Of The NPI

	HPN-1	HPN-4	Exploradores
Rignot et al. [2003]	–2.00 ± 0.29	–0.69 ± 0.31	–0.77 ± 0.22
Model set *B* (1975–2000)	–2.12	–0.17	–0.43
Model set *H* (1975–2000)	–1.99	–0.15	–0.61
Model set *I* (1975–2000)	–2.16	–0.30	–0.76
Willis et al. [2012]	–2.19 ± 0.52	–0.54 ± 0.61	–0.56 ± 0.63
Model set *B* (2000–2009)	–2.00	–0.09	–0.15
Model set *H* (2000–2009)	–1.89	–0.08	–0.32
Model set *I* (2000–2009)	–2.01	–0.21	–0.43

glaciers. Furthermore, the model's resolution of 450 m might be too low to correctly resolve all the features of these small glaciers.

[59] We simulated the surface mass balance of the NPI from 1975 to 2000 and from 2000 to 2009 in order to compare the modeled mass balance with the observed thinning rates at the non-calving glaciers in the geodetic balance surveys of *Rignot et al.* [2003] and *Willis et al.* [2012] (see section 1.1). The results of the comparison are summarized in Table 4.

[60] The annual net balances are calculated from the observed thinning by multiplying the volume losses with a density of 550 kg/m^3 for the accumulation area and 917 kg/m^3 for the ablation area for the data set of *Willis et al.* [2012] and with a density of 900 kg/m^3 for the data set of *Rignot et al.* [2003], which contained predominantly observations in the ablation area. The high thinning rates observed at HPN-1 Glacier at the western side of the NPI are reproduced as well as the moderate thinning at HPN-4 and Exploradores. At HPN-4, the model seems to overestimate systematically the annual mass balance of the glacier. This confirms the idea that there might occur snow drift from the HPN-4 Glacier to Pared Sur Glacier, which shows a very negative mass balance in the model. For the conservatively estimated errors of *Willis et al.* [2012], the simulated values for all parameter sets are within the uncertainty, whilst for the rather optimistic uncertainties of *Rignot et al.* [2003], they are within two sigma.

4.4. Calving

[61] By subtracting the modeled volume losses due to surface processes from the measured total volume losses obtained from the geodetic mass balance surveys, we can make statements about calving losses of the glaciers. In Table 5, we present the resulting calving fluxes of the two largest glaciers of the NPI, San Rafael Glacier and San Quintín Glacier, and the NPI as a whole for the two time spans 1975–2000 and 2000–2009 for the three parameter sets *B*, *H* and *I*.

[62] High calving fluxes are inferred for San Rafael Glacier and an increase of its calving fluxes is observed from 1975–2000 to 2000–2009. The inferred calving fluxes are within the range of reported fluxes for the San Rafael Glacier [*Naruse*, 1985; *Kondo and Yamada*, 1988; *Warren et al.*, 1995; *Rignot et al.*, 1996; *Koppes et al.*, 2011; *Willis et al.*, 2012. San Rafael Glacier is responsible for more than 80% of the calving fluxes of the NPI from 1975 to 2000 and more than 50% in the period 2000–2009. The calving fluxes of San Quintín Glacier are insignificant for the period 1975–2000 and at least one order of magnitude lower than that of San Rafael Glacier in 2000–2009. The calving fluxes inferred for San Quintín Glacier (2000–2009) have the same order of magnitude as the fluxes inferred from velocity measurements in February 1998 at Glacier Nef [*Warren et al.*, 2001]. The calving fluxes of NPI as a whole doubled from 1975–2000 to 2000–2009. Apart from an increase of the calving fluxes of already calving glaciers, many new glaciers began to calve into new pro-glacial lakes in the last decade. For the two large freshwater calving glaciers Nef and Steffen, the modeled annual surface mass balance was clearly lower than the measured overall mass balance in the geodetic mass balance surveys. We think that this difference between measured and modeled mass balances is also explained by snow drift mechanisms, which accumulate additional snow on these glaciers, and which are not considered in our model.

4.5. Equilibrium Line Altitudes

[63] The Equilibrium Line Altitude (ELA), the altitude of a glacier at which ablation and accumulation cancel out to a mass balance of zero, is an important glaciological variable. Together with the hypsometry, it allows for the calculation of the accumulation area ratio (AAR), which can give important information about the health state of a glacier. When the ELA agrees with the snowline at the end of the ablation season (normally late March in Patagonia), the ELA can be determined by analyzing satellite images or aerial photographs of that date. In Table 6, we compare the results of the ELAs obtained from our model with studies which inferred the ELA from the snowline at the end of the ablation season.

[64] The variation of the ELA between the different model parameter sets is low, which is expressed by the low standard deviation of the mean value. Nearly all ELAs obtained from the simulation are higher than the observed snowline altitudes at the end of the ablation season. Since the precipitation in Patagonia does not show a very strong seasonality, it seems to be very probable that there might occur snowfalls below the ELA at any time of year, which may lead to a systematic underestimation of the ELA by the observations of the snowline altitude at the end of the ablation season. The large scatter of the observed snowline altitudes at the end of the ablation season, especially at the two largest glaciers of the icefield is also interesting. The

Table 5. Inferred Calving Fluxes for the Two Largest Glaciers and the Entire Npi in Cubic-Kilometers of Ice Per Year[a]

	San Rafael	San Quintín	NPI
1975–2000			
Set *B*:	1.37 ± 0.20	–0.08 ± 0.22	2.00 ± 0.48
Set *H*:	1.29 ± 0.20	–0.07 ± 0.22	1.82 ± 0.48
Set *I*:	1.17 ± 0.20	–0.20 ± 0.22	1.52 ± 0.48
2000–2009			
Set *B*:	1.93 ± 0.02	0.05 ± 0.02	3.86 ± 0.08
Set *H*:	1.85 ± 0.02	0.16 ± 0.02	3.58 ± 0.08
Set *I*:	1.75 ± 0.02	0.08 ± 0.02	3.00 ± 0.08

[a]The uncertainties correspond to the uncertainties of the geodetic mass balance measurements. The error estimations of *Willis et al.* [2012] reduce by an order of magnitude when changing from thickness to volume errors using their assumption that individual pixel errors become uncorrelated over a distance of 630–810 m.

Table 6. Comparison of Equilibrium Line Altitudes Obtained From the Model With Values Found in Literature (Mostly by Remote Sensing)

Source	Model Mean Sets A,B,C Average 1975–2011 (m)	*Barcaza et al.* [2009] Average 5 Scenes 1979–2003 (m)	*Rivera et al.* [2007] 10 Feb 2002 (m)	*Aniya* [1988] Japanese Expeditions 1983/1984 and 1985/1986 and Aerial Photographs (m)
Grosse	1331 ± 4	1224 ± 171	1096	950
San Rafael	1203 ± 6	905 ± 10	1013	1200
San Quintín	1166 ± 6	950 ± 31	957	1200
HPN1	1125 ± 5	897 ± 376	959	1100
Steffen	1201 ± 7	1000 ± 76	1074	900–1000
Colonia	1351 ± 7	1270 ± 106	1302	1250–1300
Nef	1356 ± 5	1250 ± 140	1183	1350
Soler	1443 ± 4	1390 ± 73	1283	1350
Exploradores	1417 ± 4	1512 ± 85	1187	1250

observations of *Aniya* [1988], which are the ones that agree best with the model's results at these two glaciers, differ from the other two studies by more than 200 m. Apart from the possibility of year-round snowfall below the ELA, the differences might also be due to the large interannual variability of the mass balance, which will be discussed in the next section.

4.6. Interannual Variability of the Mass Balance

[65] In Figure 13, we present annual mass balance of the NPI as well as annual average accumulation and ablation (mean of sets *B*, *H* and *I*) for the years 1975–2011.

[66] A high interannual variability of the surface mass balance is visible. In 3 years (1975, 1990, 2009) the annual surface mass balance reaches extraordinarily high values of more than 1 m w eq. In these years, the accumulation is higher and the ablation lower than in the other years. That high accumulation coincides with low ablation is reasonable for two reasons: the high cloudiness, responsible for the high accumulation, reduces the incoming solar radiation and the additional accumulated snow takes longer to melt and increases the albedo of the NPI. A slightly increasing trend is seen in the annual surface mass balance from the 1970s and 1980s to the 1990s and 2000s, mostly due to an increase in accumulation. This may explain the similar mass loss rates of the NPI derived by *Willis et al.* [2012] for 2000–2009 and *Rignot et al.* [2003] for 1975–2000: the surface mass balance of the NPI was higher between 2000 and 2009, so were the calving losses. The purely modeled annual accumulation values (precipitation data are not an input for the reanalysis models) show a good correlation with annual precipitation values at different weather stations in the region. Here, we have to remember that the data of the weather station are calendar year sums, whereas the modeled data are hydrological years (1975 corresponding to 1 April 1975–31 March 1976).

5. Predictions of the Surface Mass Balance and Sea Level Rise in the 21st Century

[67] The simulations of the annual surface mass balance of the NPI in the 21st century using model parameter sets *B*, *H* and *I* with the downscaled ECHAM5 data as input are presented in Figure 14.

[68] Set *B* predicts slightly higher accumulation and ablation, whereas the resulting mass balance is very similar for the three model parameter sets. A marked change of the annual surface mass balance is observed from 2050 on, where it starts to decrease strongly reaching values lower than 3 m w eq towards the end of the century. This decrease of the mass balance is mainly due to an increase in the ablation, caused by increasing temperatures. The average accumulation shows a marked decrease from the 2080s on, which is due to a smaller percentage of solid precipitation. The mean annual surface mass balance changes from +0.21 m w eq in 2000–2009 to –2.35 m w eq in 2090–2099 (mean sets *B*, *H* and *I*). Summing up the annual surface mass balances, we find that mass loss of the NPI in the 21st century due to surface processes will be 282 ± 31 Gt (mean and standard deviation of sets *B*, *H* and *I*). The strong changes in annual mass change rates due to surface processes from

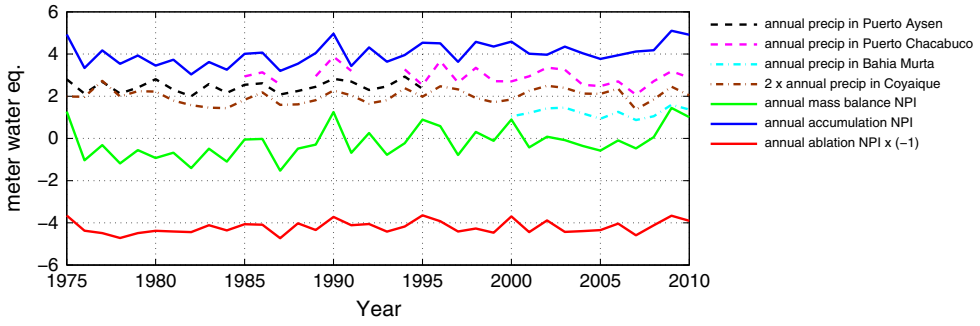

Figure 13. Modeled annual surface mass balance of the NPI and accumulation and surface ablation averaged over the NPI between 1975 and 2010 (mean values of sets *B*, *H* and *I*). Yearly precipitation data of some automatic weather stations for comparison.

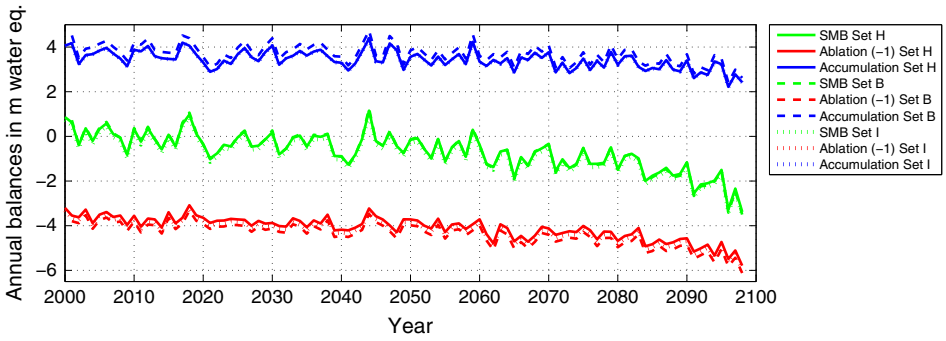

Figure 14. Modeled annual surface mass balance of the NPI and accumulation and surface ablation averaged over the NPI between 2000 and 2099.

+0.83 Gt/yr in 2000–2009 to –9.29 Gt/yr in 2090–2099 foresee much higher mass losses for the 22nd century.

[69] The contribution of losses due to calving are difficult to predict. Increasing temperatures will increase thinning, which will, together with enhanced availability of subglacial melt water, decrease the basal friction, accelerate the glaciers and increase calving fluxes. On the other hand, decreasing ice thicknesses will decrease the driving stresses and could also decrease calving fluxes in the future. Without being able to quantify these two competing processes, as a first order estimate, we assume that the calving losses in the 21st century will be the same as from 2000 to 2009 and obtain (taking the mean of the three model parameter sets in Table 5) calving losses of 310 ± 39 Gt for the NPI in the 21st century. All in all, the NPI would lose 592 ± 50 Gt of ice in the 21st century, which corresponds to a sea-level rise of 1.64 ± 0.14 mm.

6. Discussion and Conclusions

[70] In this contribution, we presented a combined modeling approach to gain new insight into the climatic situation in the region of the NPI and its surface mass balance. Geodetic and direct mass balance measurements were used to calibrate the surface mass balance model. A considerable quantity of meteorological measurements were collected and analyzed to evaluate and correct the output of the climate modeling.

[71] The average amount of annual precipitation between 1975 and 2011 of 8.03 ± 0.37 m over the NPI obtained from the combined modeling approach is slightly higher than the estimate of 6.7 of *Escobar et al.* [1992]. This can be explained by the different time span that was analyzed by *Escobar et al.* [1992] (data from the 1960s to the 1980s) and the increase of accumulation that we observe in the 1990s in our modeled data (Figure 13). An increase of accumulation in the 1990s and 2000s as compared to the second half of the 1970s and the 1980s has also been found by *Koppes et al.* [2011] on the San Rafael Glacier.

[72] The amount of yearly mass accumulation of 15.9 km^3/yr w eq obtained in this study between 1975 and 2011 is double the value estimated by *Willis et al.* [2012] over the accumulation area considering the two point accumulation values from *Yamada* [1987] and *Matsuoka and Naruse* [1999]. This is interesting, considering that our model's prediction for the mass balance is lower at the measurement location of *Yamada* [1987]. On the other hand *Willis et al.* [2012] used the mass balance value of 2.2 m/yr obtained by *Matsuoka and Naruse* [1999] on the Nef glacier, which includes modeled ablation as well instead of using the measured accumulation of 3.5 m/yr. All in all, we conclude that in the absence of meteorological data on the icefields, point measurements of mass balance are important to calibrate mass balance models, but due to the high spatial variability of accumulation and ablation processes, it is difficult to interpolate on such a large area as the NPI.

[73] Using data from the two important geodetic mass balance surveys of *Rignot et al.* [2003] and *Willis et al.* [2012] and our surface mass balance simulations, we found a strong increase of calving losses from the NPI from 1.78±0.24 km^3 of ice per year (1975–2000) to 3.76 ± 0.44 km^3 of ice per year (2000–2009). Inferred calving losses of San Rafael in 2000–2009 of 1.85 ± 0.13 km^3 are in good agreement with values found in the literature [*Koppes et al.*, 2011; *Willis et al.*, 2012]. However, velocity measurements at the calving front of San Rafael Glacier in the 1980s [*Naruse*, 1985; *Kondo and Yamada*, 1988] and the 1990s [*Warren et al.*, 1995; *Rignot et al.*, 1996] indicate that front surface velocities were similar to those measured in the 2000s [*Willis et al.*, 2012; *Maas et al.*, 2010]. Here, we must note that the velocity measurements in the 1980s and 1990s were mostly recorded in the spring and summer, whilst the measurements of *Willis et al.* [2012]; *Maas et al.* [2010] are from early autumn and therefore intra-annual variations of velocity could blur the overall increasing trend. Another possible reason for the increase in calving fluxes at San Rafael Glacier could be an increasing sliding velocity due to an increased production of melt water. An important contribution to the increase in calving losses from the NPI is the formation of new lakes at the front of formerly land terminated glaciers, e.g., Soler, Colonia, San Quintín. The calving losses of these freshwater calving glaciers on the NPI are an order of magnitude lower than the losses at San Rafael Glacier [*Warren et al.*, 2001].

[74] The surface mass balance of the NPI showed a very high interannual variability. This has to be taken account of when interpreting observations of the snowline at the end of the ablation season of one specific year as long-term equilibrium line. Comparing observations of the snowline at the end of the ablation season of different years can provide better information about the long-term ELA [*Barcaza et al.*, 2009].

Still, we found a systematic underestimation of the ELA by determining the altitude of the snowline at the end of the ablation season as compared to the results of our surface mass balance model.

[75] Our future projections of the surface mass balance of the NPI predict a strong increase in ablation from 2050 on and a decrease in accumulation from 2080, both due to an increasing temperature (Figure 4b). Assuming no significant changes in calving losses in the 21st century, we obtain an overall mass loss of 617 ± 50 Gt of ice in the 21st century, which would correspond to a sea-level rise of 1.71 ± 0.14 mm, although part of the mass losses will probably be stored in newly forming lakes and wetlands [*Loriaux and Casassa*, 2013].

[76] It is important to emphasize that the results of this study are based on a series of modeling steps, each of which comprises an important source of error and uncertainly. These errors are difficult to quantify. For the past, the results of the mass balance model can be compared to measurements to judge the performance of the model. The agreement of the model's results with measurements were mostly satisfactory, however, too negative simulated surface mass balance data were obtained for two important outlet glaciers of the NPI (Steffen and Nef). This indicates that some important processes, like, for example, snow drift, were not included in the model. In the projection of mass balance for the period until 2100, new sources of uncertainty arise. First, it must be recognized that the ECHAM5 is just one of many global models currently used to simulate future climate, and there are often considerable differences in simulations of future atmospheric warming and circulation obtained by different modeling centers [*IPCC AR4*, 2007]. Being based on just one model, our estimates of the future mass loss can only be considered to be an example of how climate change may lead to mass loss over the NPI in the future. Furthermore, ice dynamics may introduce two important new sources of error. The geometry of the icefield might change in the future: the area will reduce due to retreat, and the surface elevation will lower due to thinning. However, since the influence of both effects on the surface mass balance have different signs, the overall error could cancel out. Another important source of uncertainty caused by ice dynamics are the unknown calving fluxes in the future.

[77] In future work, a more representative estimate of future mass loss could be obtained by considering simulations from multiple GCMs under a realistic range of emissions scenarios and a detailed analysis of ice dynamical changes for at least some of the important outlet glaciers of the NPI.

[78] **Acknowledgments.** The authors would like to thank the Chilean Weather Service (Jorge Carrasco, Juan Quintana, Claudia Villarroel), the Chilean Water Directory and M. Koppes for providing meteorological data and Paulina López for providing the stake measurements at Nef Glacier. Thomas Loriaux helped with Figure 1. This study was partially sponsored by project FONDECYT 1090752. This work was supported by funding from the ice2sea programme from the European Union 7th Framework Programme, grant number 226375. Ice2sea contribution number 122.

References

Aniya, M. (1988), Glacier inventory for the Northern Patagonia Icefield, Chile, and Variations 1944/45 to 1985/86, *Arct. Alp. Res.*, *20*, 179–187.

Aniya, M., H. Sato, R. Naruse, P. Skvarca, and G. Casassa (1996), The use of satellite and airborne imagery to inventory outlet glaciers of the Southern Patagonia Icefield, South America, *Photogramm. Eng. Remote Sens.*, *62*, 1361–1369.

Aravena, J.-C., and B. H. Luckman (2009), Spatio-temporal rainfall patterns in Southern South America, *Int. J. Climatol.*, *29*, 2106–2120.

Aristarain, A., and R. Delmas (1993), Firn-core study from the Southern Patagonia Ice Cap, South America, *J. Glaciol.*, *39*, 249–254.

Barcaza, G., M. Amiya, T. Matsumoto, and T. Aoki (2009), Satellite-derived equilibrium lines in Northern Patagonia Icefield, Chile, and their implications to Glacier variations, *Arct. Antarct. Alp. Res.*, *41*, 174–182.

Bukovsky, M. S., and J. K. David (2009), Precipitation simulations using WRF as a nested regional climate model, *J. Appl. Meteorol.*, *48*, 2152–2159.

Carrasco, J., G. Casassa, and A. Rivera (2002), Meteorological and climatological aspects of the Southern Patagonia Icefield, in *The Patagonian Icefields A Unique Natural Laboratory for Environmental and Climate Change Studies*, edited by G. Cassasa, F.V. Sepúlveda, and R.M. Sinclair, 29–41, Kluwer Academic / Plenumn Publishers, New York.

Casassa, G. (1987), Ice thickness deduced from gravity anomalies on Soler Glacier, Nef Glacier and the Northern Patagonia Icefield, *Bull. Glacier Res.*, *4*, 43–57.

Chou, M.-D., and M. J. Suarez, (1994), An efficient thermal infrared radiation parameterization for use in general circulation models, *Tech. Rep.*, Laboratory for Atmospheres NASA/Goddard Space Flight Center.

Corripio, J. (2003), Vectorial algebra algorithms for calculating terrain parameters from DEMs and solar radiation modelling in mountainous terrain, *Int. J. Geogr. Inf. Sci.*, *17*, 1–23.

Escobar, F., F. Vidal, C. Garin, and R. Naruse, (1992), Water balance in the Patagonia Icefield, *Tech. Rep.*, Institute of Low Temperature Research.

Falvey, M., and R. Garreaud (2007), Wintertime precipitation episodes in central Chile: Associated meteorological conditions and orographic influences, *J. Hydrometeorol.*, *8*, 171–193.

Falvey, M., and R. D. Garreaud (2009), Regional cooling in a warming world: Recent temperature trends in the southeast Pacific and along the west coast of subtropical South America (1979–2006), *J. Geophys. Res. Atmos.*, *114*, D04102, doi:10.1029/2008JD010519.

Fowler, H. J., S. Blenkinsop, and C. Tebaldi (2007), Linking climate change modelling to impacts studies: Recent advances in downscaling techniques for hydrological modelling, *Int. J. Climatol.*, *27*, 1547–1578.

Garreaud, R., P. Lopez, M. Minvielle, and M. Rojas (2012), Large scale control on the Patagonia Climate, *J. Climate*, *26*, 215–230, doi: 10.1175/JCLI-D-12-00001.1.

Giorgi, F., and L. O. Mearns (1991), Approaches to the simulation of regional climate change: A review, *Rev. Geophys.*, *29*(2), 191–216.

Houze, R. A., Jr. (2012), Orographic effects on precipitating clouds, *Rev. Geophys.*, *50*, RG1001, doi:10.1029/2011RG000365.

Houghton, J. T., Y. Ding, D. J. Griggs, M. Noguer, P. J. van der Linden, X. Dai, K. Maskell, and C. A. Johnson (2001), *Climate Change 2001: The Scientific Basis, Contribution of Working Group I to the Third Assessment Report of the Intergovernmental Panel on Climate Change*, 28, Cambridge University Press.

Ibarzabal y Donangelo, T., J. Hoffmann, and R. Naruse (1996), Recent climate changes in Southern Patagonia, *Bull. Glacier Res.*, *14*, 29–36.

IPCC AR4 (2007), *Climate Change 2007: Contribution of Working Group I to the Fourth Assessment Report of the Intergovernmental Panel on Climate Change*, pp. 589–662, Chapter 8, Cambridge University Press, Cambridge and New York.

Jiang, Q., and R. B. Smith (2003), Cloud Timescales and Orographic Precipitation, *J. Atmos. Sci.*, *60*, 1543–1559, doi: http://dx.doi.org/10.1175/2995.1.

Kain, J., and J. Fritsch (1993), Convective parameterization for mesoscale models: The Kain-Fritsch scheme. The representation of cumulus convection in numerical models, *Meteor. Monogr.*, *46*, 165–170.

Kalnay, E., et al. (1996), The NCEP/NCAR 40 year reanalysis project, *Bull. Am. Meteorol. Soc.*, *77*, 437–471.

Kohshima, S., N. Takeuchi, J. Uetake, T. Shiraiwa, R. Uemura, N. Yoshida, S. Matoba, and M. A. Godoi (2007), Estimation of net accumulation rate at a Patagonian glacier by ice core analyses using snow algae, *Global Planet. Change*, *59*, 236–244.

Kondo, H., and T. Yamada (1988), Some remarks on the mass balance and the terminal-lateral fluctuations of San Rafael Glacier, the Northern Patagonia Icefield, *Bull. Glacier Res.*, *6*, 55–63.

Koppes, M., H. Conway, L. A. Rasmussen, and M. Chernos (2011), Deriving mass balance and calving variations from reanalysis data and sparse observations, Glaciar San Rafael, Northern Patagonia, 1950–2005, *The Cryosphere*, *5*, 791–808.

Lin, Y., S. Chiao, T. Wang, M. Kaplan, and R. Weglarz (2001), Some common ingredients for heavy orographic rainfall, *Weather Forecast.*, *16*, 633–660.

López, P., and G. Casassa (2011), Recent acceleration of ice loss in the Northern Patagonia Icefield based on an updated decennial evolution, *The Cryosphere Discuss.*, *5*, 3323–3381.

Loriaux, T., and G. Casassa (2013), Evolution of glacial lakes from the Northern Patagonia Icefield and terrestrial water storage in a sea-level rise context, *Global Planet. Change*, *102*, 33–40.

López, P., P. Chevallier, V. Favier, B. Pouyaud, F. Ordenes, and J. Oerlemans (2010), A regional view of fluctuations in glacier length in southern South America, *Global Planet. Change*, *71*, 85–108.

Maas, H.-G., G. Casassa, D. Schneider, E. Schwalbe, and A. Wendt (2010), Photogrammetric determination of spatio-temporal velocity fields at Glaciar San Rafael in the Northern Patagonian Icefield, *The Cryosphere Discuss.*, *4*, 2415–2432.

Machguth, H., F. Paul, S. Kotlarski, and M. Hoelzle (2009), Calculating distributed glacier mass balance for the Swiss Alps from regional climate model output: A methodical description and interpretation of the results, *J. Geophys. Res. Atmos.*, *114*, D19106, doi:10.1029/2009JD011775.

Masiokas, M. H., A. Rivera, L. E. Espizua, R. Villalba, S. Delgado, and J. Carlos Aravena (2009), Glacier fluctuations in extratropical South America during the past 1000 years, *Palaeogeogr. Palaeocl.*, *281*, 242–268.

Matsuoka, K., and R. Naruse (1999), Mass balance features derived from a firn core at Hielo Patagonico Norte, South America, *Arct. Antarct. Alp. Res.*, *31*, 333–340.

Mlawer, E., S. Taubman, P. Brown, M. Iacono, and S Clough (1997), Radiative transfer for inhomogeneous atmospheres: RRTM, a validated correlated-k model for the longwave, *J. Geophys. Res. Atmos.*, *102*, 16,663–16,682.

Nakajima, C. (ed.) (1985), *Glaciological Studies in Patagonia Northern Icefield*, 11, Data Center for Glacier Research, Japanese Society of Snow and Ice, Nagoya.

Naruse, R., (1985), Flow of Soler Glacier and San Rafael Glacier, *Tech. Rep.*, Data Center of Glacier Research, Japanese Society of Snow and Ice.

Naruse, R., P. Skvarca, and Y. Takeuchi (1997), Thinning and retreat of Glaciar Upsala, and an estimate of annual ablation changes in Southern Patagonia, *Ann. Glaciol.*, *24*, 38–42.

Oerlemans, J. (2001), *Glaciers and Climate Change*, 48, A.A. Balkema Publishers, Lisse, Abingdon, Exton, Tokyo.

Ohata, T., H. Enomoto, and H. Kondo, (1985), Characteristic of ablation at San Rafael Glacier, *Tech. Rep.*, Data Center of Glacier Research, Japanese Society of Snow and Ice.

Pandey, G., D. Cayan, and K. Georgakakos (1999), Precipitation structure in the Sierra Nevada of California during winter, *J. Geophys. Res. Atmos.*, *104*, 12,019–12,030.

Peña, H., and F. Escobar (1987), Aspects of glacial hydrology in Patagonia, *Bull. Glacier Res.*, *4*, 141–150.

Rasmussen, L. A., H. Conway, and C. F. Raymond (2007), Influence of upper air conditions on the Patagonia icefields, *Global Planet. Change*, *59*, 203–216.

Rignot, E., R. Foster, and B. Isacks (1996), Interferometric radar observations of Glaciar San Rafael, Chile, *J. Glaciol.*, *42*, 279–291.

Rignot, E., A. Rivera, and G. Casassa (2003), Contribution of the Patagonia Icefields of South America to sea level rise, *Science*, *302*, 434–437.

Rivera, A. (2004), Mass balance investigations at Glaciar Chico, Southern Patagonia Icefield, Chile, Ph.D. thesis, University of Bristol.

Rivera, A., T. Benham, G. Casassa, J. Bamber, and J. A. Dowdeswell (2007), Ice elevation and areal changes of glaciers from the Northern Patagonia Icefield, Chile, *Global Planet. Change*, *59*, 126–137.

Roe, G. (2005), Orographic precipitation, *Annu. Rev. Earth Planet. Sci.*, *33*, 645–671.

Roeckner, E., et al., (2003), The atmospheric general circulation model ECHAM5 Part I, *Tech. Rep.*, Max-Planck-Institut für Meteorologie.

Rosenblüth, B., G. Casassa, and H. Fuenzalida (1995), Recent climatic changes in western Patagonia, *Bull. Glacier Res.*, *13*, 127–132.

Rott, H., M. Stuefer, A. Siegel, P. Skvarca, and A. Eckstaller (1998), Mass fluxes and dynamics of Moreno Glacier, Southern Patagonia Icefield, *Geophys. Res. Lett.*, *25*, 1407–1410.

Schwikowski, M., S. Bruetsch, G. Casassa, and A. Rivera (2006), A potential high-elevation ice-core site at Hielo Patagonico Sur, *Ann. Glaciol.*, *43*, 8–13.

Shiraiwa, T., S. Kohshima, R. Uemura, N. Yoshida, S. Matoba, J. Uetake, and M. Godoi (2002), High net accumulation rates at Campo de Hielo Patagonico Sur, South America, revealed by analysis of a 45.97 m long ice core, *Ann. Glaciol.*, *35*, 84–90.

Skamarock, W. C., and J. B. Klemp (2008), A time-split nonhydrostatic atmospheric model for weather research and forecasting applications, *J. Comput. Phys.*, *227*, 3465–3485.

Smith, R. B. (1979), The influence of mountains on the atmosphere, *Adv. Geophys.*, *21*, 87–230.

Sukoriansky, S., B. Galperin, and V. Perov (2005), Application of a new spectral theory of stably stratified turbulence to the atmospheric boundary layer over sea ice, *Bound.-Lay. Meteorol.*, *117*, 231–257.

Takeuchi, Y., R. Naruse, and P. Skvarca (1996), Annual air-temperature measurement and ablation estimate at Moreno Glacier, Patagonia, *Bull. Glacier Res.*, *14*, 23–28.

Themeßl, M. J., A. Gobiet, and A Leuprecht (2011), Empirical-statistical downscaling and error correction of daily precipitation from regional climate models, *Int. J. Climatol.*, *31*, 1530–1544.

Thompson, G., P. R. Field, R. M. Rasmussen, and W. D. Hall (2008), Explicit forecasts of winter precipitation using an improved bulk microphysics scheme. Part II: Implementation of a new snow parameterization, *Mon. Weather Rev.*, *136*, 5095–5115.

Vimeux, F., M. de Angelis, P. Ginot, O. Magand, G. Casassa, B. Pouyaud, S. Falourd, and S. Johnsen (2008), A promising location in Patagonia for paleoclimate and paleoenvironmental reconstructions revealed by a shallow firn core from Monte San Valentin (Northern Patagonia Icefield, Chile), *J. Geophys. Res. Atmos.*, *113*, D16118, doi: 10.1029/2007JD009502.

Warren, C., N. Glasser, S. Harrison, V. Winchester, A. Kerr, and A. Rivera (1995), Characteristics of tide-water calving at Glaciar San-Rafael, Chile, *J. Glaciol.*, *41*, 273–289.

Warren, C., D. Benn, V. Winchester, and S. Harrison (2001), Buoyancy-driven lacustrine calving, Glaciar Nef, Chilean Patagonia, *J. Glaciol.*, *47*, 135–146.

Wilby, R., and T. Wigley (1997), Downscaling general circulation model output: A review of methods and limitations, *Prog. Phys. Geog.*, *21*, 530–548.

Wilks, D. (2006), *Statistical Methods in the Atmospheric Sciences, Second Edition (International Geophysics)*, 215–300, Chapter 7, Academic Press, Oxford, Amsterdam, Waltham, San Diego.

Willis, M. J., K. Melkonian, M. Pritchard, and J. Ramage (2012), Ice loss rates at the Northern Patagonian Icefield derived using a decade of satellite remote sensing, *Remote Sens. Environ.*, *117*, 184–198.

Wratt, D., M. Revell, M. Sinclair, W. Gray, R. Henderson, and A. Chater (2000), Relationships between air mass properties and mesoscale rainfall in New Zealand's Southern Alps, *Atmos. Res.*, *52*, 261–282.

Yamada, T. (1987), Glaciological characteristics revealed by 37.6-m deep core drilled at the accumulation area of San Rafael Glacier, the Northern Patagonia Icefield, *Bull. Glacier Res.*, *4*, 59–67.